UiO : **University of Oslo**

Florine Enengl

Investigation of Ionospheric Plasma Structuring and Processes related to Auroral Particle Precipitation

Thesis submitted for the degree of Philosophiae Doctor

Department of Physics
Faculty of Mathematics and Natural Sciences

2023

Series of dissertations submitted to the
Faculty of Mathematics and Natural Sciences, University of Oslo
No. 1234

ISSN 1234-5678

Cover: UiO.
Print production: Reprosentralen, University of Oslo.

To William and Iris

Preface

This thesis is on plasma structuring in the polar ionosphere. It comprises two articles focusing on plasma structuring processes related to auroral particle precipitation on different scales and one article on the improvement of measurement techniques to study plasma structuring processes. The collection of the three articles is the core of this thesis. The introduction guides the reader into the topic of space weather and explains how the articles contribute to the bigger picture of space weather research. It provides background on the Earth's plasma environment and the aurora, ionospheric plasma instabilities, ionospheric plasma structuring and instrumentation.

Acknowledgements

First of all, I want to thank my main supervisor, Wojciech Miloch, for his supervision and guidance through the PhD programme and my co-supervisors Lasse Clausen and Yaqi Jin for their support and fruitful discussions. I am grateful to have been part of the 4DSpace group of which I did not only find co-authors for my articles but also friends. A huge thank you to Sigvald Marholm, Daria Kotova and Sayan Adhikari. I further want thank the engineers of 4DSpace: Bjørn Lybekk, Espen Trondsen. I am glad to have carried out my PhD at the University of Oslo, and I am especially thankful to Christine Sundtveten and Andreas Görgen for supporting me to finish on time. I also appreciated the moral support of my fellow PhD colleagues: Anna Piterskaya, Steffen Brask, Pascal Sado and Lisa Buschmann. I then want to thank very kind and enthusiastic co-authors Luca Spogli, Richard Marchand and Kjellmar Oksavik. I also am grateful for those who brought me to the point of pursuing the PhD degree, here I really want to thank Nickolay Ivchenko, Noora Partamies (my Master thesis advisors) and Mika Holmberg, Fabrice Cipriani, Hugh Evans, Petteri Nieminen and others in the TEC-EPS group at ESTEC for inspiring me to pursue a space plasma physics PhD degree.

I could not have done any of this without my family: Iris, Ingrid, Klaus, William, and our cats Hammy and Sweety. I am very grateful for my friends who always believe in me and support me.

Florine Enengl
Oslo, November 2023

Abstract

This dissertation explores plasma structuring in the polar ionosphere as driven by auroral particle precipitation. Trans-ionospheric radio wave propagation is impacted by plasma structuring in the ionosphere and its effects can be observed in the received signal as recorded by ground-based scintillation receivers. The received signal disturbances, through scintillation, are thus a proxy for plasma structuring. Understanding the relation between plasma structuring and auroral particle precipitation requires studying auroral forms, intensity, and emissions at different wavelengths, which can be achieved with all-sky imagers. The combination of scintillation and optical aurora observations allows us to understand the temporal and spatial evolution of auroral forms and plasma structuring. Different filtering techniques and scintillation indices were used to understand diffractive and refractive contributions to received signal fluctuations and to classify observed plasma structuring as large (kilometers) and small-scale (hundreds to tens of meters). Knowing the scale of the processes helps to understand what instabilities are driving them. Different instabilities, such as Farley-Buneman and Kelvin-Helmholtz, were considered as possible causes of E-region plasma structuring as driven by particle precipitation.

Elevated scintillation indices were observed at the edges of auroral forms and indicate structuring predominately at the poleward edge for auroral arcs. As particle precipitation injects energy into the E-region ionosphere it takes some time for it to be redistributed. To understand which ionospheric plasma instabilities cause the observed plasma structuring, high-resolution and in-situ measurements are required. Electron density and temperature data are used to classify plasma instabilities. One way to measure them is with the use of sounding rockets, as the air density is too high for satellites to maintain their orbit in the lower ionosphere. A commonly used instrument to study plasma parameters is the Langmuir probe. In this dissertation, a method that infers high-resolution temperature data from the measured probe currents using machine learning is presented. It is the first achievement of inferring electron temperature in ionospheric conditions from synthetic data using fixed-bias Langmuir probes operating in the electron saturation region. In future work, the Langmuir probe setup, as used by UiO, can be adapted to be sensitive to the electron temperature. This enables further studies of plasma instabilities and consequent plasma structuring as driven by particle precipitation.

Sammendrag

Denne avhandlingen utforsker plasmaformasjone i polare ionosfæren, drevet av auroral partikkelnedbør. Trans-ionosfærisk radiobølgepropagasjon påvirkes av plasmaformasjonene i ionosfæren, og dens effekter kan observeres i mottatt signal som registreres av bakkebaserte scintillasjonsmottakere. Forstyrrelsene i det mottatte signalet, gjennom scintillasjon, er derfor en indirekte for plasmaformasjonene. For å forstå sammenhengen mellom plasmaformasjonene og auroral partikkelnedbør, må vi studere nordlysformasjoner, intensitet og emisjoner ved ulike bølgelengder. Dette kan oppnås med såkalte "all-sky imagers". Kombinasjonen av disse instrumentene gjør det mulig å forstå den tidsmessige og romlige utviklingen av nordlysformasjoner og plasmaformasjonene. Forskjellige filtreringsteknikker og scintillasjonsindekser ble brukt for å forstå diffraktive og refraktive bidrag til mottatte signalfluktuasjoner og å klassifisere observerte plasmaformasjonene som store og/eller småskala. Å kjenne skalaen på prosessene hjelper til med å forstå hvilke ustabiliteter som driver dem. Forskjellige ustabiliteter, som Farley-Buneman og Kelvin-Helmholtz, ble studert som årsak til E-region plasmaformasjonene, drevet av partikkelnedbør.

Forhøyede scintillasjonsindekser ble observert ved kantene av nordlysformasjoner og indikerer plasmaformasjonene hovedsakelig ved den polvendte kanten av de aurorale buene. Da partikkelnedbør overfører energi i E-regionen av ionosfæren, tar det en viss tid før det blir redistribuert. For å forstå hvilke ionosfæriske plasmaustabiliteter som forårsaker den observerte plasmaformasjonen, er høyoppløselige og in situ-målinger nødvendige. Elektrontetthets- og temperaturdata bidrar til å klassifisere plasmaustabiliteter. Et vanlig brukt instrument for å studere plasmaegenskaper er Langmuir probes. I denne avhandlingen blir en metode som finner høyoppløselige temperaturdata fra målte strømmer ved hjelp av maskinlæring, presentert. Dette er den første oppnåelsen av å finne elektrontemperatur i ionosfæriske forhold fra syntetisk data ved bruk av fast-bias Langmuir probes som opererer i elektronmetsningsområdet. I fremtidig arbeid kan Langmuir-sondeoppsettet, slik det brukes av UiO, tilpasses for å være følsomt for elektrontemperaturen. Dette muliggjør ytterligere studier av plasmaustabiliteter og påfølgende plasmaformasjonene som er drevet av partikkelnedbør.

Contents

Acronyms

Global Navigation Satellite Systems (GNSS)
Interplanetary Magnetic Field (IMF)
University of Oslo (UiO)
Gradient-Drift Instability (GDI)
Farley-Buneman Instability (FBI)
Kelvin-Helmholtz Instability (KHI)
Total Electron Content (TEC)
Ionosphere-Free Linear Combination (IFLC)
All-Sky Imager (ASI)
Longyearbyen (LYR)
Ny-Ålesund (NYA)
Hornsund (HOR)
Bjørnøya (BJN)
Hopen (HOP)
Orbital Motion Limited (OML)
multi-Needle Langmuir Probe (m-NLP)

Chapter 1

List of Publications

1.1 Publications included in the Dissertation

Paper I

Title: Ionospheric Plasma Structuring in Relation to Auroral Particle Precipitation
Authors: F. Enengl, D. Kotova, Y. Jin, L. B.N. Clausen, W. J. Miloch
Journal: *Journal of Space Weather and Space Climate*, 13, DOI: 10.1051/swsc/2022038, (Published 23 January 2023)

Paper II

Title: Investigation of Ionospheric Small-Scale Plasma Structures Associated with Particle Precipitation
Authors: F. Enengl, L. Spogli, D. Kotova, Y. Jin, K. Oksavik, N. Partamies, W.J. Miloch
Journal: *Space Weather* , DOI: 10.22541/essoar.168748399.90008606/v1, (Submitted)

Paper III

Title: Electron Temperature Inference from Multiple Fixed Bias Langmuir Probes
Authors: F. Enengl, S. Marholm, S. Adhikari, R. Marchand, W.J. Miloch
Journal: *Journal of Geophysical Research: Space Physics* , DOI: 10.1002/essoar.10512804.1, (Submitted)

1.2 Publications not included in the Dissertation

Paper IV

Title: On the Relationship of Energetic Particle Precipitation and Mesopause Temperature
Authors: F. Enengl, N. Partamies, N. Ivchenko, L. Baddeley
Journal: *Annales Geophysicae*, 39, 795–809, DOI: 10.5194/angeo-39-795-2021, (Published 9 September 2021)

Paper V

Title: Characterization of Jason-3 Spacecraft Surface Charging in LEO Polar Regions From AMBER Observations
Authors: F. Enengl, M. K.G. Holmberg, F. Cipriani, J-A. Sauvaud, D. Payan, J-C Matéo-Vélez, A. Sicard, B. Lavraud
Journal: *IEEE Transactions on Plasma Science*, 50, 4, DOI: 10.1109/TPS.2022.3157958, (Published 6 April 2022)

Paper VI

Title: Investigation of Inner Belt Flux Anisotropies
Authors: F. Enengl, H. Evans, R. B. Horne
Journal: *IEEE 21th European Conference on Radiation and Its Effects on Components and Systems (RADECS)*, DOI: 10.1109/RADECS53308.2021.9954471, (Published 23 November 2022)

Paper VII

Title: Calathus: A Sample-Return Mission to Ceres
Authors: O. Gassot, P. Panicucci, G. Acciarini, H. Bates, M. Caballero, P. Cambianica, M. Dziewiecki, Z. Dionnet, F. Enengl, S. Gerig , F. Hessinger , L. Kissick, M. Novak, C. Pellegrino, A. Pontoni, T. M. Ribeiro, C. Riegler, N. Berge, N. Huber, R. Hynek, B. Kędziora, A. Kiss, M. Martin, J. N. Montilla
Journal: *Acta Astronautica*, 181, 112-129, DOI: 10.1016/j.actaastro.2020.12.050, (Published 12 January 2021)

Paper VIII

Title: M5 – Mars Magnetospheric Multipoint Measurement Mission: A multi-spacecraft plasma physics mission to Mars
Authors: C. J. K. Larkin, V. Lundén, L. Schulz, M. Baumgartner-Steinleitner, M. Brekkum, A. Cegla, P. Dazzi, A. De Iuliis, J. Gesch, S. Lennerstrand, S. Nesbit-Östmann, V. D. C. Pires, I. T. Palanca, D. Teubenbacher, F. Enengl, M. Hallmann
Journal: *Advances in Space Research*, DOI: arXiv:2303.09502, (Submitted)

Chapter 2

Introduction

"Space weather is the physical and phenomenological state of natural space environments. The associated discipline aims, through observation, monitoring, analysis and modelling, at understanding and predicting the state of the Sun, the interplanetary and planetary environments, and the solar and non-solar driven perturbations that affect them; and also at forecasting and nowcasting the possible impacts on biological and technological systems."

– *A European definition of Space Weather, COST 724 final report, 2009* (Lilensten and Belehaki, 2009)

The Sun and interplanetary environment are linked to the near-Earth space: the Earth's magnetosphere and ionosphere. Through this link, ionospheric and magnetospheric processes driven by the solar wind can impact our technology systems in orbit and on Earth. This interaction, its effects on Earth and the current state of the space environment constitutes space weather. Space weather affects the lives of humans on many levels (Lilensten and Belehaki, 2009). It represents a significant threat to our infrastructure with wide-ranging impacts and economic cost (Eastwood et al., 2017). Space weather effects on technology can include radiation damage, single event effects, interference to spacecraft sensing systems, electrostatic charging, drag by the upper atmosphere, interference with electromagnetic signals (signal scintillation etc.), and more (Baker et al., 2004). An overview of space weather events and their effects is given in Figure 2.1. The overarching goal of space weather research is to understand, model, and forecast space weather events. This is essential to prepare for, account for, and mitigate their impacts and consequent damage to infrastructure. To eventually solve the space-weather puzzle, the near-Earth plasma environment, including the ionosphere, needs to be studied in detail.

The ionosphere is the ionized part of Earth's atmosphere. Plasma instabilities in the ionosphere can lead to multi-scale plasma structuring (Basu et al., 1990; Moen et al., 2013). Radio waves propagating through the ionosphere are impacted by the plasma structures. This can lead to phase and amplitude scintillation (rapid fluctuations), degradation of performance for Global Navigation Satellite System (GNSS) receivers and even cause loss-of-lock (Hey et al., 1946; Moen et al., 2013; Oksavik et al., 2015). Different space weather events input free energy into the ionosphere that can cause plasma instabilities and redistribution of that energy, leading to plasma structuring. During intense

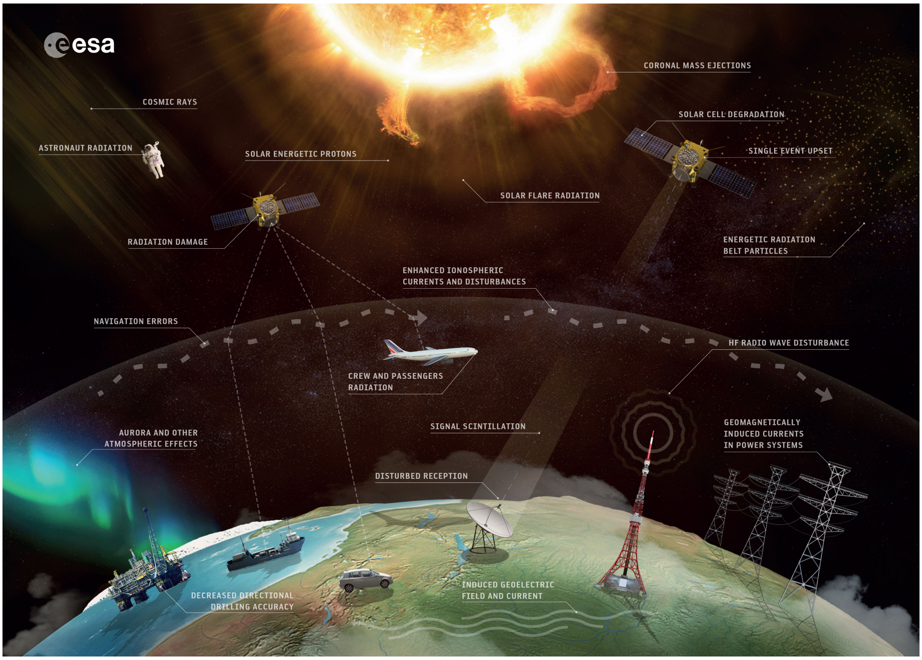

Figure 2.1: Space weather events and their effects, credit: ESA/Science Office/Operations/ Space Situational Awareness (SSA) – CC BY-SA IGO 3.0

geomagnetic activity, energetic particles precipitate into the polar ionosphere and cause auroral emissions. Auroral emissions have been linked to ionospheric irregularities and disturbances in the GNSS signals (Basu et al., 1991; Smith et al., 2008), predominately pole-ward of (Basu et al., 1998; van der Meeren et al., 2015; Oksavik et al., 2015; Conroy et al., 2022) and at the edges of auroral forms (Semeter et al., 2017). In particular, energetic particle precipitation into the ionospheric E-region is suggested to play a significant role in plasma structuring (e.g., Kinrade et al., 2013; Forte et al., 2017; Loucks et al., 2017; Sreenivash et al., 2020; Makarevich et al., 2021; Datta-Barua et al., 2021).

Ionospheric structuring through particle precipitation still has to be studied further. Pending questions in this field include: What is the spatial and temporal evolution of plasma structuring with regards to auroral emissions? Which plasma instabilities are causing the observed structuring processes? At which scales can we relate plasma structuring to particle precipitation? At which altitudes are GNSS signals impacted? How are the GNSS signals impacted? These questions need to be answered in order to understand ionospheric plasma structuring in relation to space weather events. This dissertation contributes to answering these open questions and the following findings were made in **Paper I** and **Paper II**:

- Elevated phase scintillation index values (indicating plasma structuring on large and/ or small scales) were observed to correspond to the spatial and temporal evolution of auroral forms at the altitude of green auroral emissions (557.7 nm) – the ionospheric E-region.

- Elevated amplitude scintillation index values (indicating plasma structuring on below Fresnel scale) were observed at large auroral intensity gradients, as auroral emissions are moving in/out of the line-of-sight from the satellite to the ground-based receiver. This was again observed for satellite piercing points projected onto the same altitude as green auroral emissions in the ionospheric E-region.

- The Ionosphere-Free Linear Combination, which is a measure of diffractive contributions to signal scintillation, is often elevated simultaneously with the amplitude scintillation index, suggesting the impact on the radio-wave propagation to be of diffractive nature.

- A time delay between the temporal evolution of aurora (e.g. commencement and fading of auroral activity) and elevated phase scintillation index measurements was observed. The reason may be that when particle precipitation declines or moves to a different location, it takes time for plasma structures to diffuse.

- The elevated phase scintillation index values were observed at the edges of auroral forms (for auroral spirals and bands). For discrete and stable arcs (elongated auroral form) in particular at the pole-ward edge. This is why instabilities, driven at the boundary of auroral forms, such as the Kelvin-Helmholtz instability (directly produced by a velocity shear) or the Farley-Buneman instability (through fast flows at the boundaries) may be responsible for plasma structuring.

- Significant increases in the ionospheric currents (particle precipitation) were found to contribute to plasma structuring above and below the Fresnel's scale.

To answer these questions in more detail and gain insight into processes at small scales as well as to provide foundations for space weather models and forecast services, we require detailed case studies at high-resolution and big data analyses studying long-term trends. For this we need to use state-of-the-art approaches, such as time-series analysis and machine learning techniques, to use collected data to its full potential. **Paper III** presents a method to improve in-situ plasma observations. In particular, the electron temperature was inferred by machine learning at the same (high) resolution as the synthetic current measurements by Langmuir probes, which were used as an input to a neural network. The temperature inference succeeded and a change in the multi-needle Langmuir probe configuration (a commonly used probe configuration by the University of Oslo) was proposed. At least three probes are required to infer electron temperature, density and floating potential. The changes in the probe geometry, one probe of different geometry – e.g. shorter or longer than the other two – introduce a temperature sensitivity to the multi probe system which allows to infer the temperature. A future flight with the new probe configuration in the E-region ionosphere will allow for a more specific determination of plasma parameters and instability characterization, which can then be implemented in future simulations and models to achieve the overarching goal: to forecast space weather.

Chapter 3

Background

3.1 Earth's Plasma Environment and the Aurora

A plasma is an ionized, quasineutral gas at high temperature that exhibits collective behavior (Chen, 2018). The Sun emits a continuous stream of plasma particles, the solar wind, carrying an interplanetary magnetic field (IMF). The Alfvén theorem states that the magnetic field lines (e.g. from the IMF) are 'frozen' into the plasma (e.g. solar wind) and move with it as a result of high electric conductivity (Alfvén, 1976). The Earth possesses an intrinsic magnetic dipole field of slowly varying strength and orientation in time. The IMF interacts with Earth's magnetic field and shapes the magnetosphere around the Earth. The magnetosphere is compressed by the solar wind on the sun-facing side of Earth and stretches out on the nightside. The outer boundary of the magnetosphere is the magnetopause. Magnetic reconnection occurs when magnetic fields with opposing orientation merge, forming a new magnetic field topology and releasing magnetic energy via plasma energization (Phan et al., 2000). At the dayside magnetopause, a southward pointing IMF can reconnect with the Earth's northward magnetic field and transport energy and particles into the Earth's magnetosphere. Subsequently, the solar wind particles are transported across to the night side. Reconnection of Earth's magnetic field lines can then occur in the nightside magnetotail in a process called nightside reconnection. The whole cycle is often referred to as the Dungey cycle (Cowley and Lockwood, 1992; Dungey, 1961).

The inner magnetosphere contains the ring current, flowing westward around the Earth. Most of the ring current is made up by trapped particles. Energetic and relativistic particles trapped in the inner magnetosphere are part of the radiation belts. The charged particles are subject to gyration, drift and bounce motion confining them to the radiation belt regions. The gyration motion originates from the presence of the magnetic field, the bounce motion arises from the convergence of the magnetic field (stronger magnetic field at the poles) and the longitudal drift of the particle's guiding center is due to the gradient and curvature of the near-dipole magnetic field (Chen, 2018). Partial ring currents flow around Earth only for a fraction of the ring currents, and are then coupled to Earth's ionosphere through the field-aligned (Birkeland) currents (Cowley, 2000; Kivelson and Russell, 1995), shown in Figure 3.1. The ionospheric current system further includes the Pedersen current and the Hall current. The Pedersen current links the field aligned currents. It flows perpendicular to the magnetic field and parallel to the ionospheric electric field. The Hall currents flow perpendicular to both magnetic field lines and ionospheric electric fields. Pitch-angle scattering and charge exchange are the two main processes that cause magnetospheric particles to get ‘lost’ into Earth’s atmosphere. The particles precipitate into Earth’s atmosphere. The magnetosphere is a highly dynamic system that responds to the energy input during southward IMF, i.e., when dayside reconnection is facilitated. As the IMF remains southward the ring current grows, leading to a decrease in the horizontal magnetic field component on Earth’s surface. This phenomena is named a geomagnetic storm (Kivelson and Russell, 1995).

The current impacts the magnetic field of Earth through Ampere’s law and the magnetic field variations due to the storm can therefore be measured. The storm strength can be classified according to the negative Kyoto Dst index, which is the magnetic field horizontal component perturbation at the equatorial low-latitude magnetometer stations (Sugiura, 1964). A magnetic storm can be classified as weak for a Dst index between -30 nT– -50 nT, moderate for -50 nT – -100 nT, strong for -100 nT – -200 nT and severe for under 200 nT (Loewe and Prölss, 1997; Gonzalez et al., 2007). Global disturbances of the geomagnetic field during geomagnetic storms can last for days. On the other hand, large-scale magnetotail reconnection, producing enhanced energetic particle precipitation and brightening of the aurora in the nightside high-latitude ionosphere, can take place both during and outside of a geomagnetic storm. This dramatic magnetotail reconfiguration is called a magnetospheric substorm, and it typically lasts for a couple of hours (Partamies et al., 2013). An electric field links magnetosphere to ionosphere and induces electric currents, including the auroral electrojet, which runs along the auroral oval. Magnetospheric substorms can be classified according to their auroral electrojet index, which measures the deviation of the horizontal magnetic field component (H) around the auroral oval (Davis and Sugiura, 1966). Due to the increase in the auroral electrojet, the substorm auroral breakup can be observed in the auroral oval. In this thesis, also the Kp index used to describe the state of geomagnetic disturbances. It a proxy for the energy input from the solar wind to the magnetosphere and provided by GFZ Potsdam and the National Geophysical Data Center. The Kp index is the mean value of the disturbance levels in the horizontal magnetic field components of 13 selected subauroral ground-based magnetic observatories. Higher Kp values indicate stronger geomagnetic disturbances (Matzka et al., 2021).

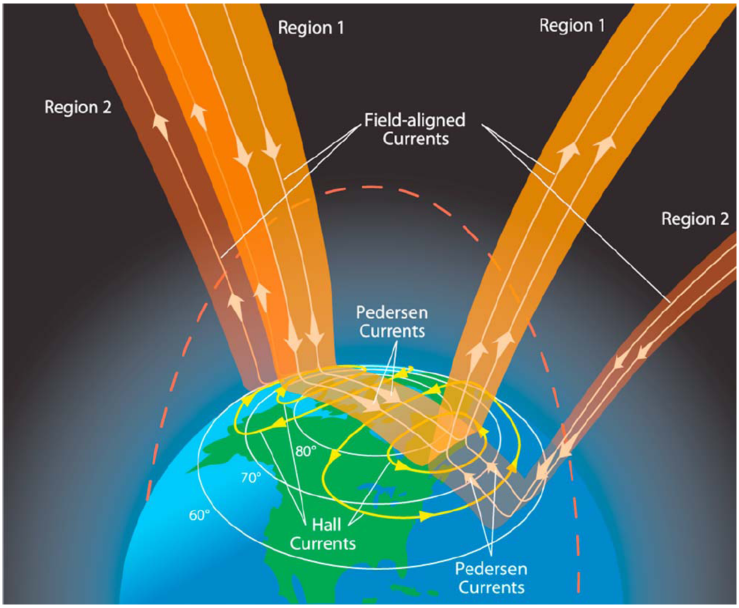

Figure 3.1: The ionospheric current system: Field-aligned currents (Birkeland currents), Pedersen currents, Hall currents. Figure 1 from Le et al. (2010).

The aurora is a signature of the direct coupling between the ionosphere and magnetosphere. Particles from the magnetosphere penetrate into the Earth's atmosphere and excite atmospheric particles resulting in auroral emissions. The precipitating particles are mostly electrons (of above 100 eV) moving along the geomagnetic field lines from the magnetosphere into the ionosphere (Partamies et al., 2015). The auroral emissions result from transitions between energy states (E_1 $[J], E_2$ $[J]$) in atoms and molecules. The wavelength of the auroral emission is then given by

$$\lambda = \frac{hc}{E_2 - E_1}. \tag{3.1}$$

An energy state transition of the atomic oxygen leads to the most characteristic emissions green (557.7 nm) and red (630 nm) at altitudes of about 130 km and 250 km respectively, while nitrogen leads to emissions in blue (427.8 nm) and violet (391.4 nm) with intensity peaks about 115 km and 120 km respectively (Brekke, 2013). Auroral emissions appear in various forms and have been categorized by their shapes, processes and lifetimes. Auroral morphology can also be related to certain substorm phases: growth, expansion and recovery (e.g., Akasofu, 1964, 1966; Elphinstone et al., 1996; Partamies et al., 2015; Oyama et al., 2017). Acceleration and loss mechanisms of particles from the radiation belts coincide with changes in the auroral morphology (Partamies et al., 2015). Auroral forms can be e.g., in the shape of an arc, curl, spiral, ray, westward

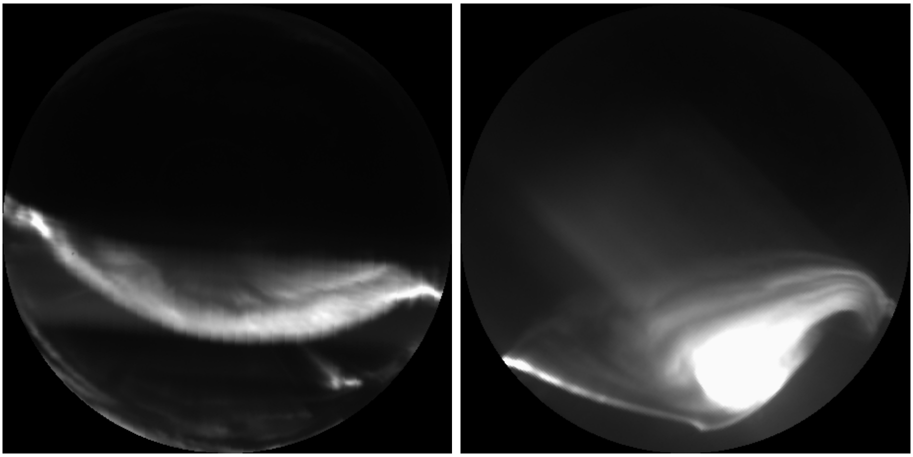

Figure 3.2: Auroral forms: arc (left panel) and spiral (right panel). The auroral arc was as observed by the UiO Longyearbyen All-sky imager on Svalbard on 23. December 2016 (at 18:34:38 UT). The auroral spiral was observed by the UiO Ny-Ålesund All-sky imager on Svalbard on 28. October 2019 (at 22:57:23 UT).

travelling surge or band (e.g., Elphinstone et al., 1996; Hallinan and Davis, 1970; Ivchenko et al., 2005; Partamies et al., 2017). An auroral arc is generated by a field-aligned sheet beam of charged particles precipitating into the atmosphere. The most simple shape is the east-west elongated, quiet, discrete auroral arc (Davis, 1978), as shown in Figure 3.2a. The width can vary from a thin arc of 0.5 km–1.5 km to mesoscale sized arcs of around 10 km–50 km (Knudsen et al., 2001; Partamies et al., 2010). The arc is a well-studied form and a review is given in Karlsson et al. (2020). Arcs often appear in tight multi-arc structures, with the arcs in parallel to one another. This makes up the most common form of discrete auroral observation (Davis, 1978; Gillies et al., 2014).

Another common form is the auroral spiral, as shown in Figure 3.2b. Spirals form as the aurora rotates counter-clockwise and have a typical size of 20 km–1300 km. Auroral forms may provide an indication of their formation process by looking at their shape. It is suggested that the Kelvin-Helmholtz instability (KHI) could play a role in formation of the spiral (Davis and Hallinan, 1976; Hallinan and Davis, 1970; Hallinan, 1976; Partamies et al., 2001). Spirals are found during magnetically disturbed periods, while arcs are found during both quiet and magnetically active times (Davis and Hallinan, 1976; Keiling et al., 2009).

3.2 Ionospheric Plasma Instabilities at High Latitudes

The Earth's ionosphere is highly variable, and it can be subject to several instabilities. The ionization in the ionosphere is due to photons and energetic particle precipitation. The primary source of ionizing radiation is the Sun. The Earth's atmosphere possesses an ionized part, called the ionosphere. Energetic particles originate directly from the Sun, magnetosphere, galactic cosmic rays, and also be due to local acceleration of ions and electrons. The ionosphere is divided vertically into three main regions, according to the degree of ionization, which also depends on region composition: the D region (below 90 km), the E region (90–130 km) and the F region (above 130 km)(Kelley, 2009; Coleman, 2017). While the ionized D region may diminish at night due to recombination of electrons with ions, the E and F region persist, even if especially the E region plasma densities weaken at night due to recombination. The main instabilities that occur in the polar ionosphere are briefly presented below.

3.2.1 Gradient-Drift Instability (GDI)

The GDI in the ionosphere is usually linked to polar cap patches and can be seen as the polar equivalent of the Rayleigh-Taylor Instability observed in the equatorial ionosphere (Ott, 1978). Polar cap patches are patches extending horizontally to more than 100 km of high plasma density that occur in the ionospheric F region. The density of a polar cap patch is at least twice the background plasma density (Weber et al., 1984; Crowley, 1996). Reconnection controls the solar-EUV ionized plasma entering the polar cap at the cusp on the dayside region. This continuous stream of dense and cold plasma (named tongue of ionization) can be cut into patches and enter the global convection pattern. The plasma material is carried by convection across the polar cap to the night side region forming high density regions of plasma, the polar cap patches (Foster et al., 2005; Moen et al., 2006, 2013, & references therein). Moving polar cap patches provide favourable conditions for the GDI. The GDI is depicted in Figure 3.3. On the positive x-axis above the boundary, the plasma density is higher (polar cap patch) than below the boundary (background plasma). This means that the density gradient ΔN is pointing in the positive x-direction. The electric field $\vec{E_0}$ is pointing in the positive y-direction, and the magnetic field $\vec{B}$ in the negative z-direction. The $\vec{E_0} \times \vec{B}$ drift is then pointing the same way as the density gradient, and the polar cap patch is moving in positive x-direction (upwards). The ions have a higher collision frequency than gyrofrequency, it is the opposite for the electrons. This leads to charge separation. The charge separation causes alternating electric fields $\vec{E_p}$ giving rise to alternating $\vec{E_p} \times \vec{B}$ drift directions amplifying the perturbations (as shown in Figure 3.3).

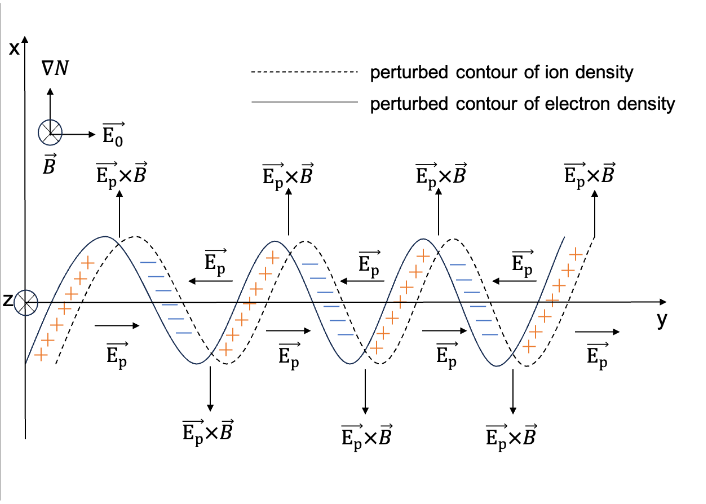

Figure 3.3: The GDI arises through the density gradient ΔN pointing in the same direction as the $\vec{E}_0 \times \vec{B}$ leading to charge separation and resulting in alternating electric fields amplifying perturbations, after Figure 21 from Tsunoda (1988)

3.2.2 Farley-Buneman Instability (FBI)

The FBI is driven by transverse currents in the collisional ionosphere. It is also referred to as the modified two-stream instability. The ions have a large ion-neutral collision frequency compared to their gyrofrequency, therefore their dynamics is effectively unmagnetized being impacted by collisions. The electrons drift past the ions, that are slower due to higher collisional cross-sections than for the electrons. The charge separation causes an alternating polarization wave electric field. The electric field speeds up particles at density wells and slows them down at density hills, amplifying the perturbations (Farley Jr., 1963; Buneman, 1963; Treumann, 1997; Dimant and Oppenheim, 2004). The E-region is subject to intense currents and electric fields of magnetospheric origin providing favourable conditions for the FBI. The FBI can cause electron heating, enhanced plasma particle transport and small-scale plasma turbulence that modify large-scale ionospheric conductance and with it the entire dynamics of the near-Earth's plasma (Dimant and Oppenheim, 2011a,b). Dimant et al. (2021) proposes that particle precipitation suppresses the FBI in the auroral region.

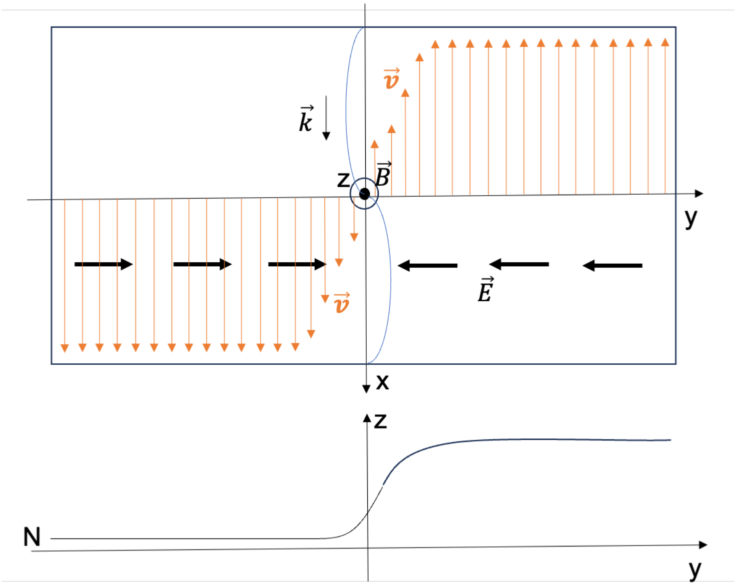

Figure 3.4: KHI caused by a velocity shear in a magnetized plasma disturbing the surface wave, based on Figure 2 from Keskinen et al. (1988)

3.2.3 Kelvin-Helmholtz Instability (KHI)

The KHI arises from shear flows in magnetized plasmas. The instability is driven by the relative streaming between the two plasmas in the presence of a magnetic field. The electric field is then given by $\vec{E} = -\vec{v} \times \vec{B}$. The two plasmas streaming past each other induce a shear flow. Across the boundary, plasma density, magnetic field and flow velocity change abruptly, see Figure 3.4. The change in the plasma pressure term is right at the boundary between the fluids. This condition allows for linear disturbance as a surface wave. The pressure disturbance fades with increasing distance from the boundary (Keskinen et al., 1988; Treumann, 1997). The auroral KHI occurs in the upper ionosphere where strong shear flows are present with perpendicular electric fields leading to $\vec{E} \times \vec{B}$ drifts. Strong shear flows along the y-axis arise due to the polarization electric field directed towards the layer, see Figure 3.4. Auroral emissions in the shape of a spiral are a known phenomenon. The curls, fluid shears in rotational shape, have been linked to the KHI (Hallinan and Davis, 1970). When looking upwards into the aurora from the northern hemisphere, the auroral electron sheet will rotate counterclockwise (Hallinan and Davis, 1970; Keskinen et al., 1988; Treumann, 1997).

3.2.4 Bump-on-Tail Instability

The fluid description for instabilities uses the assumption that there is no deviation from the thermodynamic equilibrium and velocity distributions are Maxwellian. When the velocity distributions are not Maxwellian, instabilities can be driven by the anisotropy in the velocity distribution (Chen et al., 2013). An example of a kinetic instability is the gentle beam instability. It refers to an electron beam propagating on a background plasma. The gentle beam instability has a bump-on-tail configuration in the velocity distribution as shown in Figure 3.5. The ions are seen as a fixed neutralizing background. The plasma has an electron temperature T_e, a plasma density n_0 and the thermal electron velocity v_{the}. Now a fast electron beam v_b propagates across the slower background plasma v_{the}, with a smaller density n_b and a narrow thermal speed v_{thb}. This deforms the velocity distribution. The instability will affect the part in the distribution that is changed by the electron beam. If there is a surplus of fast particles that feed energy to the wave the amplitude rises and a Langmuir wave is excited by the gentle beam instability. This process happens through inverse Landau damping (Treumann, 1997; Chen et al., 2013). If there are more slow electrons than fast ones in the Maxwellian distribution when compared to the wave velocity, dampinging of the wave occurs. The particles will take energy from the wave, dampening it. This process is referred to as Landau damping. When there is a hump on the velocity distribution, just as in Figure 3.5, the derivative of the electron velocity distribution function is positive at the hump, and the Landau damping inverts. The velocity distribution has more fast particles than slow particles at that point, a wave can be excited and its amplitude will rise at the expense of the particle energies. This is how the gentle beam instability arises and excites a Langmuir wave (Treumann, 1997; Chen et al., 2013). Langmuir waves are long wavelength, high frequency electron plasma oscillations determined by the electron inertia (Gurnett and Bhattacharjee, 2017). Particle precipitation, which can be considered as an electron beam propagating with respect to the background ionospheric plasma, is linked to kinetic instabilities.

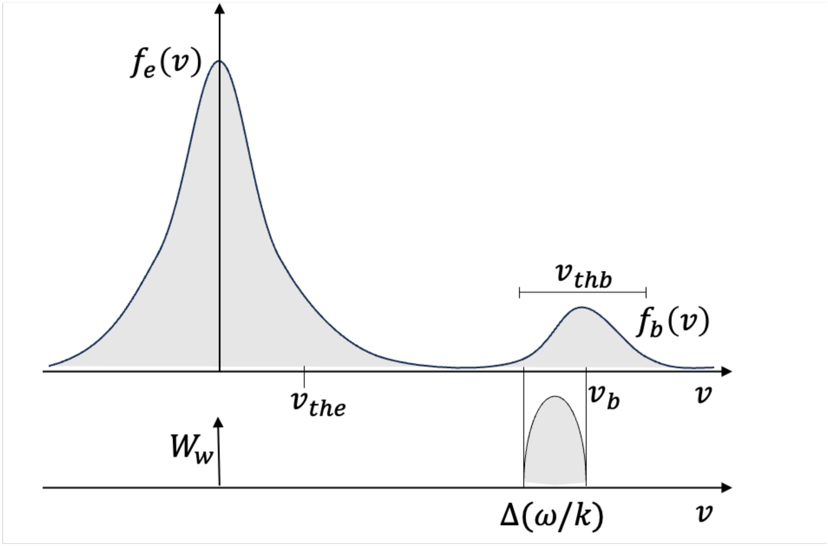

Figure 3.5: Bump-on-Tail Instability: A gentle beam (f_b, v_b) propagating on a background plasma (f_e) with thermal electron velocity (v_{the}). The instability will arise if there is a surplus of fast particles compared to the wave velocity. The amplitude of the wave grows at the expense of particle energies. Based on Figure 4.1 in Treumann (1997).

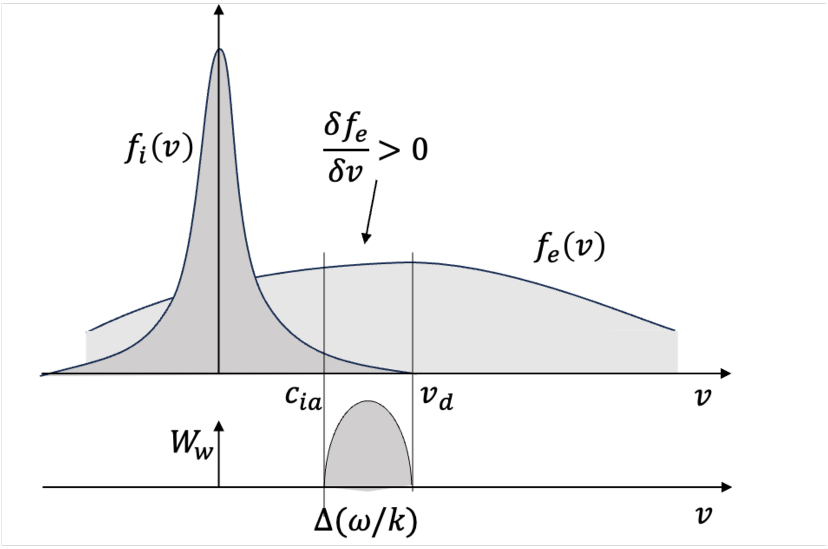

Figure 3.6: Current-driven ion acoustic instability: The combined equilibrium distribution function consists of the drifting hot electron background (f_e) and cold ions (f_i). The instability occurs if there is a positive slope ($\frac{\delta f_e}{\delta v} > 0$) in the Maxwellian distribution, meaning that a wave can feed of the energy of the particles. Based on Figure 4.3 from Treumann (1997).

3.2.5 Current- Driven Instabilities

The flow of energetic particles in field-aligned currents can also lead to current-driven instabilities (Kropotkin, 2016). The current-driven ion acoustic instability possesses, in analogy to the gentle beam instability, a background distribution with a bump in the velocity space. The background is now made up of drifting hot electrons with Maxwellian distribution superposed with cold immobile ions. There is a positive slope where resonance can occur between waves and particles, as shown in Figure 3.6. The instability can arise out of the positive slope region in the electron distribution function. Strong field-aligned currents can excite the current-driven ion acoustic waves of several tenths of meter wavelength along the magnetic field. They lead to fluctuations of plasma density irregularities along the auroral field lines in the upper ionosphere (Treumann, 1997). The current-driven instability is also suggested to be responsible for the small-scale structures of discrete aurora due to small-scale transverse structures in the flows of auroral electrons (Kropotkin, 2016).

3.3 Ionospheric Plasma Structuring and its Effects on Radio wave Propagation

The polar cap is the region surrounding the geomagnetic pole, at which the field lines are open and are connected to the solar wind. The auroral oval is found equatorward of the polar cap and is a region of closed field lines (Burrell et al., 2020). The auroral oval stretches down to 78° on the sunward side and down to about 67° on the anti-sunward side. It is fixed with respect to the sun, but not static as it widens and retracts (Brekke, 2013). The Birkeland currents are connecting the magnetosphere to the ionosphere in the auroral oval. The polar cap and auroral oval are regions associated with significant structuring of electron plasma density (Jin et al., 2019), and these structures can disturb propagation of radio waves. The cusp, which is a small area in the polar cap next to the open-closed field lines around local magnetic noon, is often highly structured, due to particle precipitation and flow shears, and hence can be associated with scintillation of radio waves (Pitout and Bogdanova, 2021). When moving south due to increased geomagnetic activity, the cusp allows intake of high density dayside plasma into the polar cap. This high density plasma often forms so-called tongue of ionisation and polar cap patches, which are ‘islands’ of enhanced density being convected towards the night time auroral oval. While convecting in the polar cap, they are subject to GDI, which leads to significant structuring and hence the increased phase scintillations (Moen et al., 2013). However, the strongest scintillations have been found when polar cap patches coinciding with particle precipitation and flow shears. This is during their formation in the cusp and when they exit the polar cap and enter the auroral oval (Jin et al., 2017). Even when directly comparing auroral arcs, polar cap patches and auroral blobs in the polar ionosphere, the polar cap patches transforming into auroral blobs were associated with the strongest irregularities in the F-region and corresponding scintillation (Jin, Yaqi et al., 2014; Jin et al., 2016). Studies of the nightside auroral oval show that severe and localized plasma structuring is observed at the edges of aurora during substorms in the E-region (van der Meeren et al., 2015; Enengl et al., 2023). It has also been demonstrated that field-aligned currents can play an essential role for severe plasma structuring in the dayside auroral region (Fæhn Follestad et al., 2020). Particle precipitation, flow shears and polar cap patches provide free energy to the ionosphere causing plasma instabilities and irregularities (e.g., Tsunoda, 1988; Kelley et al., 1982; Moen et al., 2013; van der Meeren et al., 2015; Spogli et al., 2016; Jin et al., 2016, 2017; Fæhn Follestad et al., 2020). The free energy is redistributed into different scales through plasma instabilities (Basu et al., 1998; Moen et al., 2013; Dimant et al., 2021). The listed phenomena are a part of space weather, and they potentially impact critical infrastructure such as communication and positioning systems. Thus, there are many plasma structuring mechanisms that can occur at the same time, in particular close to the boundary regions. These include, for example, GDI and KHI that act on larger scales, due to plasma configuration in space. When subject to auroral particle precipitation, other instabilities can also contribute to the structuring. The current-convective instability and ion cyclotrone instability are associated with current systems (Ossakow and Chaturvedi, 1979). While there can also be present secondary instabilities, leading to broadband turbulence, it is often difficult to determine the dominant mechanism leading to structuring (Spicher et al., 2015, 2016).

The ionosphere can act as a duct to transmit radio waves around the globe. As radio waves encounter the ionosphere, they can be reflected back to the ground and from there reflected back to the ionosphere. In that way, radio waves can travel considerable distances. This is still used for civilian and military purposes. However, using communication and navigation satellites is nowadays a more preferred option. Radio waves above 50 MHz penetrate the ionosphere. To reach beyond the ionosphere and to avoid substantial effects on the propagation path, frequencies above 100 MHz are used for satellite operations. However, plasma is dispersive and so is the plasma in the ionosphere with respect to GNSS signals. The ionosphere will therefore still affect the signal causing a phase advance, group delay, Doppler shift and polarization, among others (Coleman, 2017; Hofmann-Wellenhof et al., 2007). Radio waves at a frequency range of 100 MHz–4 GHz are scattered by plasma irregularities and structures in the ionosphere (Basu et al., 1988; Basu and Groves, 2001). An electromagnetic wave propagating through a medium has a frequency f. The phase refractive index n_{ph} in the medium is then given by:

$$n_{ph} = 1 + \frac{c_2}{f^2}, \tag{3.2}$$

when cutting off the series expansion after the quadric term. The coefficient c_2 depends on the electron density n_e along the propagation path (Seeber, 2003). The group refractive index n_{gr} is given by $\frac{dn_{ph}}{df}$. The group and phase velocity can be calculated with $\frac{c}{n}$, with c_2 being approximately $-40.3\ n_e$. As n_e is positive, this results in a group delay and phase advance. Fermat's principle gives the measured range s integrated along signal path:

$$s = \int n ds, \tag{3.3}$$

and the geometric range s_0 (direct line of sight) by setting the refractive index $n = 1$. The difference between the measured and geometric range is then the refractive correction term:

$$R = \int n ds - \int ds_0. \tag{3.4}$$

Inserting the expression for the refractive index n, the coefficient c_2 and approximating the integration of the first term with the geometric range, results in:

$$R_{gr} = -\int \frac{c_2}{f^2} ds_0 = \frac{40.3}{f^2} \int n_e ds_0. \tag{3.5}$$

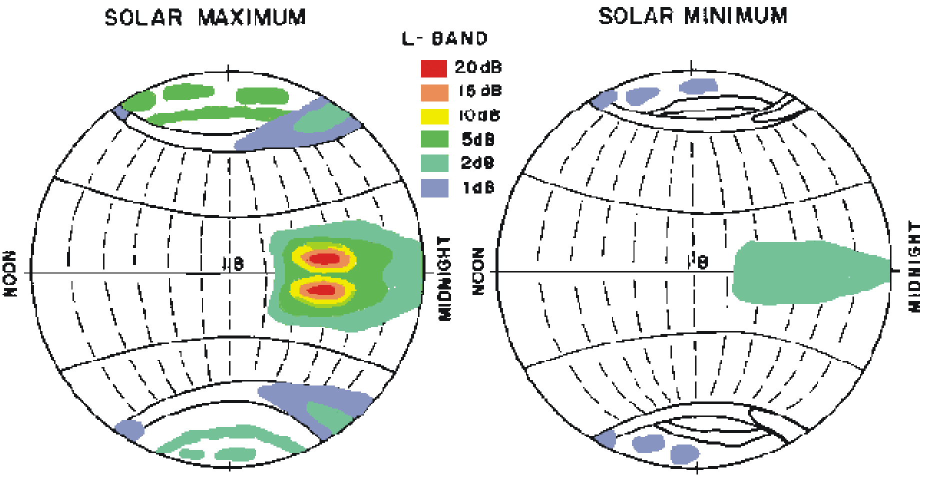

Figure 3.7: Scintillation of L-Band frequencies during solar maximum (left) and solar minimum (right). Figure 1 from Basu and Groves (2001).

This incorporates the definition of the total electron content (TEC):

$$\mathrm{TEC} = \int n_e ds_0. \tag{3.6}$$

Ionospheric impact is mostly eliminated by the use of dual frequencies. The use of dual frequencies means that the GNSS satellites emit at least two carrier waves (Hofmann-Wellenhof et al., 2007). Electromagnetic waves propagating through a medium encounter diverse effects. Attenuation is defined as the decreasing power with increasing distance from the emitter and is a function of the refractive index, geometrical spreading and absorption. Besides attenuation of the signal, also fading and scintillation occurs. Fading describes the temporal variation of signal power, variation of attenuation of the signal with the properties in a medium. Scintillation describes power variations due to alternating physical characteristics along the signal path causing fluctuations in amplitude and phase (Hofmann-Wellenhof et al., 2007). The effect of ionospheric plasma structuring on trans-ionospheric radio wave propagation, that is difficult to account for, is scintillation. It is observed that in a relative motion between the satellite, the ionosphere and the receiver, temporal fluctuations of intensity and phase are imprinted in the received signal. Scintillation refers to the rapid fluctuations of the phase and amplitude as observed by ground-based receivers (Hey et al., 1946; Basu and Groves, 2001; Kintner et al., 2007). In the equatorial ionosphere even stronger scintillations are observed than in the high latitude ionosphere (Basu et al., 1988), see Figure 3.7.

Plasma irregularities can cause degradation of the receiver tracking performance. Total Electron Content (TEC) jumps can lead to cycle slips and loss-of-lock (Skone et al., 2001; Alfonsi et al., 2008; Moen et al., 2013; Oksavik et al., 2015; Chernyshov et al., 2020, & references therein). Scintillation receivers can be used to probe the ionospheric plasma and understand when and where plasma irregularities happen and why. Indications of plasma structuring at different scales can be determined, e.g., by calculating the amplitude scintillation index (S_4) and phase scintillation index (σ_ϕ). While the σ_ϕ index could indicate plasma structuring at any scale, the S_4 index indicates structuring at and below the Fresnel scale. The Fresnel zone is defined as an ellipsoid around the line of sight from satellite to receiver, incorporating the area that contributes to the signal arriving at the receiver. The Fresnel scale F_r is the radius of the Fresnel zone and defined by the wavelength of the signal λ and the irregularity layer height z the signal is propagating through for propagation distances $s >> z$:

$$F_r = \sqrt{2\lambda z} \tag{3.7}$$

(Rino and Fremouw, 1977). The received signal is usually detrended with a 6th-order highpass Butterworth filter, using a cutoff frequency of 0.1 Hz to remove slow variations due to satellite motion (Fremouw et al., 1978). A cutoff angle is then applied to avoid multipath effects.

The amplitude scintillation index S_4 is a measure for small-scale plasma structuring and is calculated by:

$$S_4 = \sqrt{\frac{\langle I^2 \rangle - \langle I \rangle^2}{\langle I \rangle^2}}, \tag{3.8}$$

with I being the signal intensity. The S_4 index describes plasma irregularities at and below the Fresnel radius (in a range of hundreds of meters to tens of meters) (e.g., Basu et al., 1998; Kintner et al., 2007). Amplitude scintillations are due to diffraction. Refraction does impact the wave path and power, but will not cause amplitude fluctuations (McCaffrey and Jayachandran, 2019). The phase scintillation index σ_ϕ is a proxy for plasma structuring on large and small scales and given by:

$$\sigma_\phi = \sqrt{\langle \phi^2 \rangle - \langle \phi \rangle^2}. \tag{3.9}$$

It is the standard deviation of the detrended measured phase (Yeh and Liu, 1982; Kintner et al., 2007). Elevated σ_ϕ can be caused by ionospheric irregularities at small wave numbers produced by fluctuations of plasma density integrated along the signal path. This contribution to the σ_ϕ index is classified as refractive. When caused near the first Fresnel radius as the result of interference between different phases, the phase scintillations can be thought of as diffractive (Kintner et al., 2007). The origin of the phase scintillation measured on ground is the sum of the refractive and diffractive contribution. The refractive part of the signal is deterministic, and can be accounted for. The diffractive part is stochastic (Kintner et al., 2007; McCaffrey and Jayachandran, 2019). Refraction is observed for small and large scale structures, while diffraction occurs for structures equal or below the Fresnel scale (Kintner et al., 2007; Zheng, Yuhao et al., 2022).

As a cutoff frequency of 0.1 Hz for low frequency refractive contributions does not eliminate all refractive effects in the signal. A combination of two signals can be used to eliminate the first-order refractive contribution, named the ionosphere-free linear combination (IFLC) (Carrano et al., 2013). The IFLC is calculated using a combination of two carrier phases of the received waves at different frequencies (f_1 and f_2). It accounts for the bulk of the refractive contribution induced by the ionosphere on the phase measurements (McCaffrey and Jayachandran, 2019). The refractive correction term R was given in equation 3.5 (Kashcheyev et al., 2012; Zheng, Yuhao et al., 2022). The two different carrier frequencies are assumed to take the same propagation path from satellite to receiver $d_{s1} = d_{s2}$. The refractive correction term ratio of two carrier waves is then given by

$$\frac{R_1}{R_2} = \frac{f_1^2}{f_2^2}. \tag{3.10}$$

The carrier phase variations L_ϕ at a constant frequency depend on the signal wavelength λ, the integer ambiguity N and the geometric distance r:

$$L_\phi = r + \lambda N - R. \tag{3.11}$$

Finally, the IFLC can be expressed without dependency on the refractive index correction term using two frequencies and corresponding carrier phases ϕ_{L1} and ϕ_{L2}:

$$IFLC = \frac{f_{c1}^2 \phi_{L1} - f_{c2}^2 \phi_{L2}}{f_{c1}^2 - f_{c2}^2} = r + \frac{f_{c1}^2}{f_{c1}^2 - f_{c2}^2}\lambda N - \frac{f_{c2}^2}{f_{c1}^2 - f_{c2}^2}\lambda N, \tag{3.12}$$

It is non-refractive and used as a measure for diffraction (Cordes et al., 1986; McCaffrey and Jayachandran, 2019; Carrano et al., 2013; Zheng, Yuhao et al., 2022). In relation to plasma structuring, the σ_ϕ index indicates structuring processes on large and/or small-scales, while the S_4 index indicates below Fresnel-scale/ small-scale plasma structuring. In addition, the IFLC can be used to differentiate between refractive and diffractive events.

Chapter 4

Instrumentation

To measure ionospheric plasma conditions, a variety of instruments can be used. Some instruments are used for probing the ionosphere in-situ, while others monitor it from ground or further away in space. Static instruments have an advantage of long statistical time-series analysis and provide a large series of data for selecting case studies under specific conditions. Continuous measurements and large data sets help understanding large-scale dynamics, evolution and data trends. In-situ instruments provide high-resolution measurements and are used to understand physical processes in detail. Combining multiple instruments and data sets help to unravel multi-scale processes. This is what is needed to study ionospheric plasma. Ground-based instrumentation used for space weather research includes radars, imagers, ionosondes, lidars and scintillation receivers. In this dissertation the most important ground-based instruments are: scintillation receivers and all-sky cameras. They are further described in this section.

Besides the ground-based instrumentation, in-situ plasma characterization measurements are necessary to study plasma structuring and instabilities. To measure in-situ plasma parameters, a satellite or rocket has to pass right through the plasma and record data. Sounding rockets are able to probe the ionosphere, where the atmospheric density is too high for satellites to maintain their orbits. They also travel at lower velocity and can therefore sample at higher spatial resolution than satellites. Typical instruments for plasma measurements on rockets include: magnetometers, electric field probes and Langmuir probes. For resolving small-scale plasma processes the sampling resolution is crucial. This is why in this dissertation high-resolution electron temperature inference from Langmuir probe set-ups was studied. To provide the reader with a background, Langmuir probes are introduced in detail in this section.

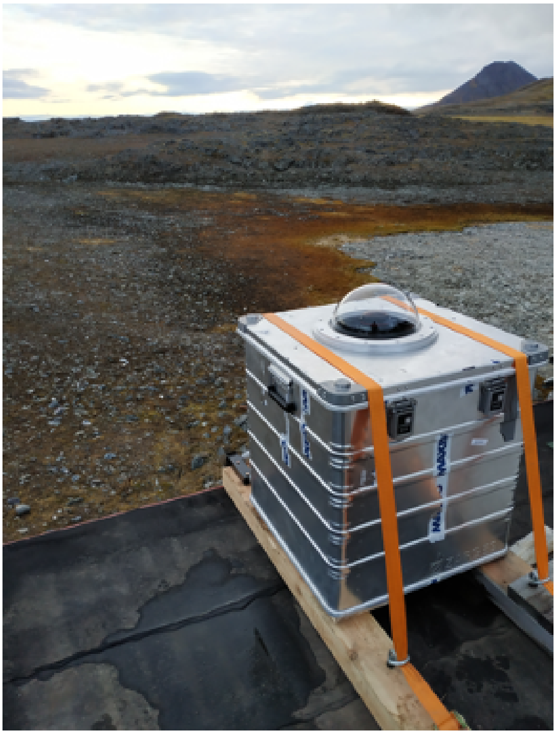

Figure 4.1: All-Sky Camera in Hornsund, Svalbard. Photo by Wojciech Miloch.

4.1 All-Sky Imager

The all-sky imager (ASI) is a camera with fish-eye shaped lens capturing a field-of-view of 180° often with filters at specific wavelength. The University of Oslo operates multiple all-sky imagers on Svalbard. The imagers are situated in Longyearbyen (LYR, geographic coordinates: 78.15° N, 16.04° E) and in Ny-Ålesund (NYA, geographic coordinates 78.92° N, 11.93° E). An image example from the LYR and the NYA ASI is shown in Figure 3.2. The imagers are Keo Sentry 4ix Monochromatic Imagers from Keo Scientific. They are equipped with the narrow band filters to observe the 557.7 nm (green) and 630.0 nm (red) auroral emissions. The imager in Hornsund (HOR, geographic coordinates 77° N, 15.55° E) is a Sony A7 SII color camera enclosed in a camera case, shown in Figure 4.1. The green auroral emissions are optimally projected to an altitude between 110 km–140 km (Partamies et al., 2022; Whiter et al., 2023), while the red auroral emissions auroral are normally projected to an altitude of around 200 km–250 km (Jackel et al., 2004). Triangulation techniques with multiple imagers can be used for precise mapping of the emissions.

4.2 Ionospheric Scintillation Monitor Receivers

GNSS receivers receive signals from the navigation satellites. Besides their use for satellite-positioning services, they can, if adequately designed, be used as Ionospheric Scintillation Monitor Receivers (ISMRs) for space weather research as they can monitor TEC and scintillation. Some are developed specifically for space weather purposes and provide phase and intensity data at high sampling frequencies. They can receive signals on different frequencies and from different GNSS constellations. Different satellite signals from GALILEO, GPS and GLONASS have previously been shown to be similarly affected by ionospheric irregularities (van der Meeren et al., 2015; Alfonsi et al., 2016). In this dissertation, multiple scintillation receivers are used.

NovAtel GPStation-6 receivers are operated by the University of Oslo and University of Bergen. They provide pre-processed 1-min scintillation indices that are used in this dissertation. The University of Oslo operates NovAtel GPStation-6 receivers on Svalbard, close to the ASI in Hornsund and Ny-Ålesund. Further receivers situated in Ny-Ålesund and Longyearbyen are operated by the University of Bergen, again in proximity to the ASIs. Other receivers from the University of Bergen are placed on Bjørnøya (BJN, geographic coordinates 74.50° N, 19° E) and Hopen (HOP, geographic coordinates 76.51° N, 25.01° E) (Oksavik, 2020). The Septentrio PolaRxS/PolaRx5s ISMR provides high-resolution phase and intensity data, up to 100 Hz, and real-time pre-processed scintillation indices. A Septentrio PolaRxS/PolaRx5s scintillation receiver operated by the National Institute of Geophysics and Volcanology (Italy) is situated at Longyearbyen, Svalbard (geographic coordinates: 78.17° N, 16° E). High-resolution (50 Hz) multi-frequency data from this receiver was used in this dissertation. The amplitude, phase and frequency data was post-processed to calculate scintillation indices on 1-second intervals and multi-frequency data was exploited to determine refractive contributions to the signal. This provides the opportunity to study plasma structuring at even higher resolution. For the post-processing, a Butterworth Filter was used. The Butterworth filter is a maximally flat-response filter, aiming for a even sensitivity ('flat') for frequencies of interest (in the pass-band) and rejecting not-needed frequencies (in the stop-band). The roll-off is the slope at which the filter responds between pass- and stop-band. It is given by the order of the Butterworth filter. The transfer function H is the ratio between output and input signal in the frequency domain. It represents the Laplace transform (generalisation of the continuous Fourier transform) of the analog impulse response, including feedback and weighing coefficients. For the high-pass Butterworth filter it is given by

$$|H|^2 = \frac{1}{1 + \frac{\Omega}{\Omega_c}^{-2N}}, \tag{4.1}$$

with Ω being the frequencies (in radians per second), Ω_c the cut-off frequency and N the filter order. When used as a high-pass filter, it passes through signals above the cut-off frequency and attenuates the signals with frequencies below the cut-off frequency (Butterworth, 1930; Alessio, 2016).

4.3 Langmuir Probes

In this dissertation, a method was developed to infer electron temperature from specific fixed-bias Langmuir probe setups. A Langmuir probe is a biased conductor placed into a plasma collecting a current (Mott-Smith and Langmuir, 1926). Stepping through a pre-defined set of voltages, whilst measuring the current produces the current–voltage (I–V) curve that can be used to derive the plasma parameters, see Figure 4.2. V_p denotes the plasma potential and V_b the probe bias. If the probe bias is now much larger than the plasma potential, an electron current I_e is collected as positive particles are repelled. The corresponding region on the I–V curve is called the electron saturation region. If the probe bias is much smaller than the plasma potential, an ion current I_i is collected, this happens in the ion saturation region. In the transition region (electron retardation region), electron and ion currents are collected due to higher thermal velocity of the electrons, see again Figure 4.2. The floating potential V_f is where the ion and electron currents are equal, as according to Kirchhoff's law the net current is zero.

The current collected by the probe depends on the probe size with respect to the characteristics length scale in plasma, which is the Debye length. The Debye length is determined by the temperature and density of charged particles. It denotes the sheath thickness that arises out of displacement when a charged test particle placed in a homogenous plasma. Particles of the opposite species will shield the test particle (ions will be attracted by an electron, electrons will be repelled), the shielding is named Debye shielding (Gurnett and Bhattacharjee, 2017). For sufficiently long probes with radii smaller than the Debye length (in the thick sheath limit), the currents are collected according to the orbital motion limited (OML) theory. In the OML theory, particle trajectories must fulfill the conservation of energy and angular momentum, and the background plasma is assumed to be non-drifting, Maxwellian and unmagnetized (Mott-Smith and Langmuir, 1926).

A particle travelling in the vicinity of a spherical probe, will be attracted or repelled by the probe when approaching it. The impact parameter h denotes the distance from the probe center in which charged particle trajectories will be impacted. It is given by the conservation of angular momentum and energy:

$$h = r\sqrt{1 - \frac{2e\phi}{m\vec{v}}}, \tag{4.2}$$

with the probe radius r, particle velocity $\vec{v}$ at the sheath, particle mass m and the potential ϕ at the probe (Lai, 2011). The total current collected on the

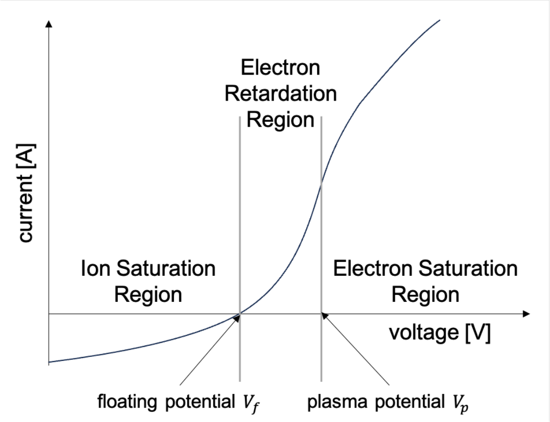

Figure 4.2: Current-Voltage curve showing ion saturation, electron retardation (transition region) and electron saturation region.

spherical probe with charge q, density n and velocity $\vec{v}$ is given by

$$dI = 4\pi h^2 nq\vec{v}f(\vec{v})d\vec{v}. \tag{4.3}$$

Integrating over the Maxwellian velocity distribution gives following expression for the currents of the attracted species I_a and the repelled species I_r to a spherical probe:

$$I_a = 4\pi r^2 nq\sqrt{\frac{kT}{2\pi m}}(1 + \frac{q\phi}{kT}). \tag{4.4}$$

$$I_r = 4\pi r^2 nq\sqrt{\frac{kT}{2\pi m}}e^{-\frac{q\phi}{kT}}. \tag{4.5}$$

The parameters k, q, m_e, A, T are the Boltzmann constant, the elementary charge, the electron mass, the probe surface area and particle temperature respectively. Dependent on the probe bias voltage, a particle species will be attracted or repelled. The operation regime is chosen according to what parameters should be measured. In the electron saturation region, electron current is measured, ion current is negligible, and it is possible to derive electron temperature and density. The collected electron current I_c for different probe types in the electron saturation regime according to OML is then given by:

$$I_c = An_e q\sqrt{\frac{kT_e}{2\pi m_e}}C\left(1 + \frac{q(V_f + V_b)}{kT_e}\right)^{\beta}, \tag{4.6}$$

with the electron temperature T_e, the electron density n_e, $V_f + V_b$ the sum of floating and bias voltage. For a cylindrical probe the geometry constant C is defined as $2/\sqrt{\pi}$ and for a spherical probe C is set to 1, in the OML regime. β is a parameter dependent on the probe geometry and plasma parameters (it is assumed that $\beta = 0$ for planar probes, $\beta = 0.5$ for finite-length cylinders and $\beta = 1$ for spheres)(Mott-Smith and Langmuir, 1926). However, as we discuss in **Paper III**, the assumed values for β are different for variations in length and radii of the probes.

A high-resolution Langmuir probe sampling concept for multiple probes in the electron saturation regime was developed by the University of Oslo, named the multi-needle Langmuir probe (m-NLP). It does not sweep through probe bias voltages, but rather uses multiple fixed bias Langmuir probes with pre-defined bias voltages to produce a high-resolution I–V curve, of which plasma parameters can be calculated from (Jacobsen et al., 2010; Bekkeng et al., 2010). **Paper III** presents proposed changes to the m-NLP to enable electron temperature inference.

Chapter 5

Articles

This chapter incorporates the summary of the three articles on which this thesis is based on. Their key findings are presented and potential future work is outlined.

5.1 Summary of Articles

In **Paper I** the role of auroral particle precipitation in ionospheric plasma structuring is discussed. Multi-point measurements from scintillation receivers and all-sky imagers from Longyearbyen, Ny-Ålesund and Hornsund on Svalbard are used to observe the temporal and spatial evolution of auroral forms and σ_ϕ values (a proxy for large-scale plasma structuring). Three precipitation events with similar background conditions (substorm events, particle precipitation) showing clear strong auroral emissions were selected. Here we studied two stable arcs, two dynamic auroral bands and a spiral. For all studied forms, the elevated σ_ϕ values correspond to the spatial and temporal evolution of auroral emissions when an ionospheric piercing point for navigation satellites aligns with the estimated altitude of the green auroral emissions (557.7 nm). The green auroral emission altitude is within the ionospheric E-region and therefore may be the altitude at which plasma structuring leading to elevated σ_ϕ driven by auroral particle precipitation originates. We further observed a time delay between the temporal evolution of aurora (e.g. commencement and fading of auroral activity) and elevated σ_ϕ measurements. As particle precipitation enhances the plasma density it will still take some time for the plasma structures to diffuse when the precipitation stops. Instabilities will continue to cause a redistribution of energy and irregularity dissipation. For discrete and stable arcs, elevated σ_ϕ values are predominately observed pole-ward, and for faster moving shapes, including spirals and bands, on the boundaries of the form. Plasma structuring can be directly driven at the boundary of auroral forms through E-region instabilities, e.g. the Kelvin-Helmholtz instability (directly produced by a velocity shear such as from particle precipitation) or Farley-Buneman instability (through fast flows at the boundaries).

Paper II builds upon **Paper I**. In this paper the aim is to understand the relation of small-scale structuring and particle precipitation. The 50 Hz scintillation receiver data was used for a high-resolution analysis of the temporal evolution of S_4 (a proxy for small-scale plasma structuring) and an all-sky imager to record corresponding auroral emissions. We, again, chose precipitation events with similar background conditions (particle precipitation, strong auroral emissions, ongoing geomagnetic activity). Clear increases in the S_4 values were observed at large auroral intensity gradients, e.g. at the commence and fading of auroral intensity as the auroral emissions are is moving in and out of the line of sight of the satellite to the receiver. This suggests that significant changes in auroral particle precipitation and hence intensification of ionospheric currents contributes to structuring below the Fresnel scale. The IFLC (diffractive contribution of the phase) often corresponds to elevated S_4 index values and indicates a diffractive nature of the events. After researching small and large-scale plasma structuring related to auroral particle precipitation the next step is to verify the proposed drivers for structuring through precipitation. One instability that was highlighted in both articles to drive plasma structuring processes is the Farley-Buneman instability. In-situ measurements can be used to characterize the plasma conditions and the instabilities growth rates. The electron temperature is a crucial parameter to describe plasma processes and has not yet successfully been inferred from the m-NLP measurements, as often used by sounding rockets. This is the motivation for **Paper III**.

Paper III presents a new method on electron temperature inference in ionospheric conditions from synthetic data from fixed bias Langmuir probe setups using machine learning at high-resolution. The electron temperature was inferred at the same rate as the currents are sampled by the probes. The probe setup required adaptions from the m-NLP. Using three probes, with one probe of different length/ geometry from the other two, is the key to enable temperature sensitivity of the probe setup. By changing the length/ radius, the probe setup can be optimized. We constructed synthetic data sets consisting of calculated collected currents from probes, corresponding to parameters representative of ionospheric plasma to train a neural network and verify the results with a test set. The validity of the approach was further verified by using data from the International Reference Ionosphere. Implementing the proposed changes to the m-NLP design will provide the possibility to study ionospheric plasma instabilities in higher resolution than before and add the missing link to understand plasma structuring in the ionosphere.

5.2 Outlook

Paper I focuses on plasma structuring driven by particle precipitation and is used as the first paper in this dissertation. It builds up onto previous articles stating that a variety of highly dynamic phenomena (e.g., polar cap patches, field aligned currents, high density F region plasma, or particle precipitation) cause plasma irregularities in the E and F region ionosphere (e.g., Moen et al., 2013; van der Meeren et al., 2015; Spogli et al., 2016; Jin et al., 2016, 2017; Fæhn Follestad et al., 2020). Further studies indicate that the pole-ward edge of the auroral oval may be the source for elevated scintillation indices (e.g., Kinrade et al., 2013; van der Meeren et al., 2015; Semeter et al., 2017). It is known that auroral particle precipitation can lead to significant plasma irregularities (e.g., Kelley et al., 1982; Keskinen and Ossakow, 1983; Weber et al., 1985; Prikryl et al., 2011), but it is still an open question to what extent it contributes to plasma structuring and whether it is dominant in the E or F-region ionosphere. **Paper I** provides in-depth case studies to evaluate whether auroral particle precipitation is a main driver of E-region plasma structuring. **Paper II** is the natural continuation of the preceding paper, presenting a study on plasma structuring at higher resolution and on smaller scales. The study goal was to understand the relation of auroral particle precipitation and small-scale plasma structuring. The receiver data used in this paper was processed by own algorithm. This was done in order to stay in control of the filtering algorithms and detect changes on finer scales. Furthermore, the contribution of diffractive and refraction effects on the phase were assessed using the IFLC. Refractive contributions to scintillation are currently heavily discussed (e.g., McCaffrey and Jayachandran, 2019; Ghobadi et al., 2020; Conroy et al., 2022). **Paper III**, unlike its predecessors, primarily focuses on a new method to infer electron temperature from fixed-bias Langmuir probe setups rather than understanding the effects of particle precipitation on trans-ionospheric radio wave propagation. This can in the future be used to characterize plasma instabilities using high-resolution in-situ measurements. In the conclusions of **Paper I** and **Paper II** diverse plasma instabilities are suggested to play a role in ionospheric plasma structuring. To confirm the proposed instabilities, high-resolution and in-situ measurements will be required. **Paper III** is building up on previous work from Barjatya et al. (2009) and Hoang et al. (2018), who used non-linear fits, radial basis functions and machine learning techniques for plasma parameter inference and Marholm (2020), who suggested a change of the probe geometry to enable temperature inference. **Paper III** succeeds in developing a method for high-resolution electron temperature inference. From this perspective, **Paper III** lays the path to future work to continue understanding plasma structuring in the E-region ionosphere in relation to particle precipitation. This contributes to the main future goal: forecasting space weather. The question on how particle precipitation relates to plasma structuring has not yet been fully answered. Further studies based on this dissertation could be:

1. Statistical studies at high spatial and temporal resolution investigating the time-delay. Quantifying the time delay between auroral emissions and scintillation onset contributes to understanding the processes causing the delay and is useful for forecasting space weather effects.

2. Case studies at high spatial and temporal resolution to understand the plasma structuring and time-delay process.

3. In-situ case studies and simulations to investigate plasma instabilities, such as Kelvin-Helmholtz/ Farley-Buneman etc., as a cause for E-region large-scale plasma structuring by particle precipitation. This can be done to verify which of the proposed instabilities lead to the observed plasma structuring.

4. Multi-instrument case studies to understand the combination of simultaneous large-scale and small-scale structuring as driven by auroral particle precipitation and their spatial and temporal evolution.
5. Statistical studies using high-resolution scintillation receiver data to study the cause and nature of elevated scintillation indices and the effect of plasma structuring on trans-ionospheric radio waves.
6. Development and testing of methods and instruments to measure plasma parameters at high-resolution and resolve instability growth rates.
7. Expand the method of high-resolution temperature inference for the m-NLP adaptation including magnetic field effects and intermediate sphere sizes, in order to reliably infer temperature from future missions.
8. Apply suggested m-NLP adaptations to acquire in-situ high-resolution electron temperature data from rocket experiments to characterize plasma instabilities during auroral particle precipitation.

Bibliography

Akasofu, S.-I., 1964. The development of the auroral substorm. *Planetary and Space Science*, **12**(4), 273–282. https://doi.org/10.1016/0032-0633(64)90151-5. 3.1

Akasofu, S.-I., 1966. The auroral oval, the auroral substorm, and their relations with the internal structure of the magnetosphere. *Planetary and Space Science*, **14**(7), 587–595. https://doi.org/10.1016/0032-0633(66)90043-2. 3.1

Alessio, S. M., 2016. Digital signal processing and spectral analysis for scientists. Signals and Communication Technology. Springer International Publishing : Imprint: Springer, Cham, 1st ed. 2016. edn. ISBN 3-319-25468-5. https://doi.org/10.1007/978-3-319-25468-5. 4.2

Alfonsi, L., P. J. Cilliers, V. Romano, I. Hunstad, E. Correia, et al., 2016. First observations of GNSS ionospheric scintillations from DemoGRAPE project. *Space Weather*, **14**(10), 704–709. https://doi.org/10.1002/2016SW001488. 4.2

Alfonsi, L., A. J. Kavanagh, E. Amata, P. Cilliers, E. Correia, et al., 2008. Probing the high latitude ionosphere from ground-based observations: The state of current knowledge and capabilities during IPY (2007-2009). *Journal of Atmospheric and Solar-Terrestrial Physics*, **70**(18, SI), 2293–2308. https://doi.org/10.1016/j.jastp.2008.06.013. 3.3

Alfvén, H., 1976. On frozen-in field lines and field-line reconnection. *Journal of Geophysical Research (1896-1977)*, **81**(22), 4019–4021. https://doi.org/10.1029/JA081i022p04019. 3.1

Baker, D. N., E. Daly, I. Daglis, J. G. Kappenman, and M. Panasyuk, 2004. Effects of space weather on technology infrastructure. *Space Weather*, **2**(2). https://doi.org/10.1029/2003SW000044. 2

Barjatya, A., C. M. Swenson, D. C. Thompson, and K. H. Wright, 2009. Data analysis of the floating potential measurement unit aboard the international space station. *Review of scientific instruments*, **80**(4), 041,301–041,301–11. https://doi.org/10.1063/1.3116085. 5.2

Basu, S., S. Basu, E. Costa, C. Bryant, C. E. Valladares, and R. C. Livingston, 1991. Interplanetary magnetic field control of drifts and anisotropy of high-latitude irregularities. *Radio Science*, **26**(4), 1079–1103. https://doi.org/10.1029/91RS00586. 2

Basu, S., and K. M. Groves. Specification and forecasting of outages on satellite communication and navigation systems, 423–430. American Geophysical Union

(AGU), 2001. ISBN 9781118668351. https://doi.org/10.1029/GM125p0423. 3.3, 3.7, 3.3

Basu, S., E. MacKenzie, and S. Basu, 1988. Ionospheric constraints on VHF/UHF communications links during solar maximum and minimum periods. *Radio science*, **23**(3), 363–378. https://doi.org/10.1029/RS023i003p00363. 3.3, 3.3

Basu, S., E. Mackenzie, S. Basu, W. R. Coley, J. R. Sharber, and W. R. Hoegy, 1990. Plasma structuring by the gradient drift instability at high latitudes and comparison with velocity shear driven processes. *Journal of Geophysical Research*, **95**(A6), 7799–7818. https://doi.org/10.1029/JA095iA06p07799. 2

Basu, S., E. J. Weber, T. W. Bullett, M. J. Keskinen, E. MacKenzie, P. Doherty, R. Sheehan, H. Kuenzler, P. Ning, and J. Bongiolatti, 1998. Characteristics of plasma structuring in the cusp/cleft region at Svalbard. *Radio Science*, **33**(6), 1885–1899. https://doi.org/10.1029/98RS01597. 2, 3.3, 3.3

Bekkeng, T. A., K. S. Jacobsen, J. K. Bekkeng, A. Pedersen, T. Lindem, J.-P. Lebreton, and J. I. Moen, 2010. Design of a multi-needle Langmuir probe system. *Measurement Science and Technology*, **21**(8), 085,903. https://doi.org/10.1088/0957-0233/21/8/085903. 4.3

Brekke, A. Physics of the upper polar atmosphere. Springer Berlin Heidelberg : Imprint: Springer, Berlin, Heidelberg, 1st ed. 2013. edn., 2013. ISBN 1-283-94625-4. https://doi.org/10.1007/978-3-642-27401-5. 3.1, 3.3

Buneman, O., 1963. Excitation of field aligned sound waves by electron streams. *Physical review letters*, **10**(7), 285–287. https://doi.org/10.1103/PhysRevLett.10.285. 3.2.2

Burrell, A. G., G. Chisham, S. E. Milan, L. Kilcommons, Y.-J. Chen, E. G. Thomas, and B. Anderson, 2020. AMPERE polar cap boundaries. *Annales Geophysicae*, **38**(2), 481–490. https://doi.org/10.5194/angeo-38-481-2020, URL https://angeo.copernicus.org/articles/38/481/2020/. 3.3

Butterworth, S., 1930. On the theory of filter amplifiers. **7**(1), 536–541. 4.2

Carrano, C. S., K. M. Groves, W. J. McNeil, and P. H. Doherty, 2013. Direct measurement of the residual in the ionosphere-free linear combination during scintillation. In Proceedings of the 2013 international technical meeting of the Institute of Navigation, 585–596. 3.3, 3.3

Chen, F. F., 2018. Introduction to plasma physics and controlled fusion. Springer International Publishing, Cham, third edition. edn. ISBN 9783319223094. https://doi.org/10.1007/978-3-319-22309-4. 3.1

Chen, L., D. J. Wu, and J. Huang, 2013. Kinetic Alfvén wave instability driven by field-aligned currents in a low- plasma. *Journal of Geophysical Research. Space physics*, **118**(6), 2951–2957. https://doi.org/10.1002/jgra.50332. 3.2.4

Chernyshov, A. A., W. J. Miloch, Y. Jin, and V. I. Zakharov, 2020. Relationship between TEC jumps and auroral substorm in the high-latitude ionosphere. *Scientific Reports*, **10, 6363**. https://doi.org/10.1038/s41598-020-63422-9. 3.3

Coleman, C., 2017. Analysis and modeling of radio wave propagation. Cambridge University Press, Cambridge. ISBN 1-316-81190-5. https://doi.org/10.1017/9781316798607. 3.2, 3.3

Conroy, J. P., K. Deshpande, W. Scales, and A. Zaghloul, 2022. Statistical analysis of refractive and diffractive scintillation at high latitudes. *Radio Science*, **57**(2), e2021RS007,259. https://doi.org/10.1029/2021RS007259. 2, 5.2

Cordes, J. M., A. Pidwerbetsky, and R. V. E. Lovelace, 1986. Refractive and diffractive scattering in the interstellar medium. , **310**, 737. https://doi.org/10.1086/164728. 3.3

Cowley, S., and M. Lockwood, 1992. Excitation and decay of solar wind-driven flows in the magnetosphere-ionosphere system. In Annales Geophysicae, vol. 10, 103–115. 3.1

Cowley, S. W. H. Magnetosphere-ionosphere interactions: A tutorial review, 91–106. American Geophysical Union (AGU), 2000. ISBN 9781118669006. https://doi.com/10.1029/GM118p0091. 3.1

Crowley, G., 1996. Critical review of ionospheric patches and blobs. *in Review of Radio Science 1993–1996*, (27), 619–648. 3.2.1

Datta-Barua, S., P. Llado Prat, and D. L. Hampton, 2021. Multi-year detection, classification and hypothesis of ionospheric layer causing GNSS scintillation. *Radio Science*, **56**(12), e2021RS007,328. https://doi.org/10.1029/2021RS007328. 2

Davis, T., 1978. Observed characteristics of auroral forms. *Space Science Reviews*, **22**(1), 77–113. https://doi.org/10.1007/BF00215814. 3.1

Davis, T. N., and T. J. Hallinan, 1976. Auroral spirals, 1. Observations. *Journal of Geophysical Research*, **81**(22), 3953–3958. https://doi.org/10.1029/JA081i022p03953. 3.1

Davis, T. N., and M. Sugiura, 1966. Auroral electrojet activity index AE and its universal time variations. *Journal of Geophysical Research (1896-1977)*, **71**(3), 785–801. https://doi.org/10.1029/JZ071i003p00785. 3.1

Dimant, Y., and M. Oppenheim, 2004. Ion thermal effects on E-region instabilities: linear theory. *Journal of Atmospheric and Solar-Terrestrial Physics*, **66**(17), 1639–1654. 40 Years of Equatorial Aeronomy Sparked by the Jicamarca Radio Observatory, https://doi.org/10.1016/j.jastp.2004.07.006. 3.2.2

Dimant, Y. S., G. V. Khazanov, and M. M. Oppenheim, 2021. Effects of electron precipitation on E-region instabilities: theoretical analysis. *Journal of Geophysical Research: Space Physics*, **126**(12), e2021JA029,884. https://doi.org/10.1029/2021JA029884. 3.2.2, 3.3

Dimant, Y. S., and M. M. Oppenheim, 2011a. Magnetosphere-ionosphere coupling through E region turbulence: 1. Energy budget. *Journal of Geophysical Research: Space Physics*, **116**(A9). https://doi.org/10.1029/2011JA016648. 3.2.2

Dimant, Y. S., and M. M. Oppenheim, 2011b. Magnetosphere-ionosphere coupling through E region turbulence: 2. Anomalous conductivities and frictional heating. *Journal of Geophysical Research: Space Physics*, **116**(A9). https://doi.org/10.1029/2011JA016649. 3.2.2

Dungey, J. W., 1961. Interplanetary magnetic field and the auroral zones. *Physical Review Letters*, **6**(2), 47–48. https://doi.org/10.1103/PhysRevLett.6.47. 3.1

Eastwood, J. P., E. Biffis, M. A. Hapgood, L. Green, M. M. Bisi, R. D. Bentley, R. Wicks, L.-A. McKinnell, M. Gibbs, and C. Burnett, 2017. The economic impact of space weather: Where do we stand? *Risk Analysis*, **37**(2), 206–218. https://doi.org/10.1111/risa.12765. 2

Elphinstone, R. D., J. S. Murphree, and L. L. Cogger, 1996. What is a global auroral substorm? *Reviews of Geophysics*, **34**(2), 169–232. https://doi.org/10.1029/96RG00483. 3.1

Enengl, F., D. Kotova, Y. Jin, L. B. Clausen, and W. J. Miloch, 2023. Ionospheric plasma structuring in relation to auroral particle precipitation. *J. Space Weather Space Clim.*, **13**, 1. 10.1051/swsc/2022038, URL https://doi.org/10.1051/swsc/2022038. 3.3

Farley Jr., D. T., 1963. A plasma instability resulting in field-aligned irregularities in the ionosphere. *Journal of Geophysical Research*, **68**(22), 6083–6097. https://doi.org/10.1029/JZ068i022p06083. 3.2.2

Forte, B., C. Coleman, S. Skone, I. Häggström, C. Mitchell, F. Da Dalt, T. Panicciari, J. Kinrade, and G. Bust, 2017. Identification of scintillation signatures on GPS signals originating from plasma structures detected with EISCAT incoherent scatter radar along the same line of sight. *Journal of Geophysical Research: Space Physics*, **122**(1), 916–931. https://doi.org/10.1002/2016JA023271. 2

Foster, J. C., A. J. Coster, P. J. Erickson, J. M. Holt, F. D. Lind, et al., 2005. Multiradar observations of the polar tongue of ionization. *Journal of Geophysical Research: Space Physics*, **110**(A9). https://doi.org/10.1029/2004JA010928. 3.2.1

Fremouw, E. J., R. L. Leadabrand, R. C. Livingston, M. D. Cousins, C. L. Rino, B. C. Fair, and R. A. Long, 1978. Early results from the DNA wideband satellite experiment—complex-signal scintillation. *Radio Science*, **13**(1), 167–187. https://doi.org/10.1029/RS013i001p00167. 3.3

Fæhn Follestad, A., K. Herlingshaw, H. Ghadjari, D. J. Knudsen, K. A. McWilliams, J. I. Moen, A. Spicher, J. Wu, and K. Oksavik, 2020. Dayside field-aligned current impacts on ionospheric irregularities. *Geophysical Research Letters*, **47**(11), e2019GL086,722. https://doi.org/10.1029/2019GL086722. 3.3, 5.2

Ghobadi, H., L. Spogli, L. Alfonsi, C. Cesaroni, A. Cicone, et al. Disentangling ionospheric refraction and diffraction effects in GNSS raw phase through fast iterative filtering technique, vol. 24. John Wiley Sons, New York, NY :, 2020. https://doi.org/10.1007/s10291-020-01001-1. 5.2

Gillies, D. M., D. J. Knudsen, E. F. Donovan, E. L. Spanswick, C. Hansen, D. Keating, and S. Erion, 2014. A survey of quiet auroral arc orientation and the effects of the interplanetary magnetic field. *Journal of Geophysical Research: Space Physics*, **119**(4), 2550–2562. https://doi.org/10.1002/2013JA019469. 3.1

Gonzalez, W. D., E. Echer, A. L. Clua-Gonzalez, and B. T. Tsurutani, 2007. Interplanetary origin of intense geomagnetic storms (Dst $<$ 100 nT) during solar cycle 23. *Geophysical research letters*, **34**(6), L06,101–n/a. https://doi.org/10.1023/A:1005160129098. 3.1

Gurnett, D. A., and A. Bhattacharjee, 2017. Introduction to plasma physics : with space, laboratory and astrophysical applications. https://doi.org/10.1017/9781139226059. 3.2.4, 4.3

Hallinan, T. J., 1976. Auroral spirals, 2. Theory. *Journal of Geophysical Research*, **81**(22), 3959–3965. https://doi.org/10.1029/JA081i022p03959. 3.1

Hallinan, T. J., and T. Davis, 1970. Small-scale auroral arc distortions. *Planetary and Space Science*, **18**(12), 1735–1736. https://doi.org/10.1016/0032-0633(70)90007-3. 3.1, 3.1, 3.2.3

Hey, J. S., S. J. Parsons, and J. W. Phillips, 1946. Fluctuations in cosmic radiation at radio-frequencies. *Nature (London)*, **158**(4007), 234–234. https://doi.org/10.1038/158234a0. 2, 3.3

Hoang, H., K. Røed, T. A. Bekkeng, J. I. Moen, A. Spicher, L. B. N. Clausen, W. J. Miloch, E. Trondsen, and A. Pedersen, 2018. A study of data analysis techniques for the multi-needle Langmuir probe. *Measurement Science and Technology*, **29**(6), 065,906. https://doi.org/10.1088/1361-6501/aab948. 5.2

Hofmann-Wellenhof, B., H. Lichtenegger, and E. Wasle, 2007. GNSS — global navigation satellite systems: GPS, GLONASS, Galileo, and more. Springer Vienna, Vienna. ISBN 9783211730126. https://doi.org/10.1007/978-3-211-73017-1. 3.3, 3.3

Ivchenko, N., E. M. Blixt, and B. S. Lanchester, 2005. Multispectral observations of auroral rays and curls. *Geophysical Research Letters*, **32**(18). https://doi.org/10.1029/2005GL022650. 3.1

Jackel, B. J., F. Creutzberg, E. F. Donovan, and L. L. Cogger, 2004. Triangulation of auroral red-line emission heights. *Scientific and technical aerospace reports*, **42**(4). 4.1

Jacobsen, K. S., A. Pedersen, J. I. Moen, and T. A. Bekkeng, 2010. A new Langmuir probe concept for rapid sampling of space plasma electron density. *Measurement science technology*, **21**(8), 085,902–085,902. https://doi.org/10.1088/0957-0233/21/8/085902. 4.3

Jin, Y., J. I. Moen, W. J. Miloch, L. B. N. Clausen, and K. Oksavik, 2016. Statistical study of the GNSS phase scintillation associated with two types of auroral blobs. *Journal of geophysical research. Space physics*, **121**(5), 4679–4697. https://doi.org/10.1002/2016JA022613. 3.3, 5.2

Jin, Y., J. I. Moen, K. Oksavik, A. Spicher, L. B. Clausen, and W. J. Miloch, 2017. GPS scintillations associated with cusp dynamics and polar cap patches. *Journal of Space Weather and Space Climate*, **7**, A23. https://doi.org/10.1051/swsc/2017022. 3.3, 5.2

Jin, Y., A. Spicher, C. Xiong, L. B. N. Clausen, G. Kervalishvili, C. Stolle, and W. J. Miloch, 2019. Ionospheric Plasma Irregularities Characterized by the Swarm Satellites: Statistics at High Latitudes. *Journal of Geophysical Research: Space Physics*, **124**(2), 1262–1282. https://doi.org/10.1029/2018JA026063. 3.3

Jin, Yaqi, Moen, Jøran I., and Miloch, Wojciech J., 2014. GPS scintillation effects associated with polar cap patches and substorm auroral activity: direct comparison. *J. Space Weather Space Clim.*, **4**, A23. https://doi.org/10.1051/swsc/2014019. 3.3

Karlsson, T., L. Andersson, D. Gillies, K. Lynch, O. Marghitu, N. Partamies, N. Sivadas, and J. Wu, 2020. Quiet, discrete auroral arcs–observations. *Space Science Reviews*, **216**(1). https://doi.org/10.1007/s11214-020-0641-7. 3.1

Kashcheyev, A., B. Nava, and S. M. Radicella, 2012. Estimation of higher-order ionospheric errors in GNSS positioning using a realistic 3-D electron density model. *Radio Science*, **47**(4). https://doi.org/10.1029/2011RS004976. 3.3

Keiling, A., V. Angelopoulos, J. Weygand, O. Amm, E. Spanswick, et al., 2009. THEMIS ground-space observations during the development of auroral spirals. *Annales Geophysicae*, **27**(11), 4317–4332. https://doi.org/10.5194/angeo-27-4317-2009. 3.1

Kelley, M. C., 2009. The earth's ionosphere : plasma physics and electrodynamics, vol. 96 of *International geophysics series*. Academic Press, San Diego, 2nd ed. edn. ISBN 9780120884254. https://doi.org/10.1016/B978-0-12-404013-7.X5001-1. 3.2

Kelley, M. C., J. F. Vickrey, C. W. Carlson, and R. Torbert, 1982. On the origin and spatial extent of high-latitude F region irregularities. *Journal of Geophysical Research: Space Physics*, **87**(A6), 4469–4475. https://doi.org/10.1029/JA087iA06p04469. 3.3, 5.2

Keskinen, M. J., H. G. Mitchell, J. A. Fedder, P. Satyanarayana, S. T. Zalesak, and J. D. Huba, 1988. Nonlinear evolution of the Kelvin-Helmholtz instability in the high-latitude ionosphere. *Journal of Geophysical Research: Space Physics*, **93**(A1), 137–152. https://doi.org/10.1029/JA093iA01p00137. 3.4, 3.2.3

Keskinen, M. J., and S. L. Ossakow, 1983. Theories of high-latitude ionospheric irregularities: A review. *Radio science*, **18**(6), 1077–1091. https://doi.org/10.1029/RS018i006p01077. 5.2

Kinrade, J., C. N. Mitchell, N. D. Smith, Y. Ebihara, A. T. Weatherwax, and G. S. Bust, 2013. GPS phase scintillation associated with optical auroral emissions: First statistical results from the geographic South Pole. *Journal of Geophysical Research: Space Physics*, **118**(5), 2490–2502. https://doi.org/10.1002/jgra.50214. 2, 5.2

Kintner, P. M., B. M. Ledvina, and E. R. de Paula, 2007. GPS and ionospheric scintillations. *Space weather*, **5**(9). https://doi.org/10.1029/2006SW000260. 3.3, 3.3, 3.3

Kivelson, M., and C. Russell, 1995. Introduction to space physics. Cambridge University Press, Cambridge. ISBN 0521451043. https://doi.org/10.1017/9781139878296. 3.1

Knudsen, D. J., E. F. Donovan, L. L. Cogger, B. Jackel, and W. D. Shaw, 2001. Width and structure of mesoscale optical auroral arcs. *Geophysical Research Letters*, **28**(4), 705–708. https://doi.org/10.1029/2000GL011969. 3.1

Kropotkin, A., 2016. Formation of the small-scale structure of auroral electron precipitations. *Journal of Atmospheric and Solar-Terrestrial Physics*, **148**, 39–47. https://doi.org/10.1016/j.jastp.2016.08.009. 3.2.5

Lai, S. T., 2011. Fundamentals of Spacecraft Charging: Spacecraft Interactions with Space Plasmas. Princeton University Press, Princeton. ISBN 9780691129471. 4.3

Le, G., J. A. Slavin, and R. J. Strangeway, 2010. Space Technology 5 observations of the imbalance of regions 1 and 2 field-aligned currents and its implication to the cross-polar cap Pedersen currents. *Journal of Geophysical Research: Space Physics*, **115**(A7). https://doi.org/10.1029/2009JA014979. 3.1

Lilensten, J., and A. Belehaki, 2009. Developing the scientific basis for monitoring, modelling and predicting space weather. *Acta geophysica*, **57**(1), 1–14. https://doi.org/10.2478/s11600-008-0081-3. 2

Loewe, C. A., and G. W. Prölss, 1997. Classification and mean behavior of magnetic storms. *Journal of Geophysical Research: Space Physics*, **102**(A7), 14,209–14,213. https://doi.org/10.1029/96JA04020. 3.1

Loucks, D., S. Palo, M. Pilinski, G. Crowley, I. Azeem, and D. Hampton, 2017. High-latitude GPS phase scintillation from E region electron density gradients during the 20–21 December 2015 geomagnetic storm. *Journal of Geophysical Research: Space Physics*, **122**(7), 7473–7490. https://doi.org/10.1002/2016JA023839. 2

Makarevich, R. A., G. Crowley, I. Azeem, C. Ngwira, and V. V. Forsythe, 2021. Auroral E-Region as a source region for ionospheric scintillation. *Journal of Geophysical Research: Space Physics*, **126**(5), e2021JA029,212. https://doi.org/10.1029/2021JA029212. 2

Marholm, S., 2020. The unstructured particle-in-cell method with applications for objects in ionospheric plasmas. PhD dissertation, University of Oslo. URL https://www.duo.uio.no/bitstream/handle/10852/73029/1/PhD-Marholm-2020.pdf. 5.2

Matzka, J., C. Stolle, Y. Yamazaki, O. Bronkalla, and A. Morschhauser, 2021. The Geomagnetic Kp Index and Derived Indices of Geomagnetic Activity. *Space weather*, **19**(5). https://doi.org/10.1029/2020SW002641. 3.1

McCaffrey, A. M., and P. T. Jayachandran, 2019. Determination of the refractive contribution to GPS phase "scintillation". *Journal of Geophysical Research: Space Physics*, **124**(2), 1454–1469. https://doi.org/10.1029/2018JA025759. 3.3, 3.3, 3.3, 5.2

Moen, J., H. C. Carlson, K. Oksavik, C. P. Nielsen, S. E. Pryse, H. R. Middleton, I. W. McCrea, and P. Gallop, 2006. EISCAT observations of plasma patches at sub-auroral cusp latitudes. *Annales Geophysicae*, **24**(9), 2363–2374. https://doi.org/10.5194/angeo-24-2363-2006. 3.2.1

Moen, J., K. Oksavik, L. Alfonsi, Y. Daabakk, V. Romano, and L. Spogli, 2013. Space weather challenges of the polar cap ionosphere. *Journal of Space Weather and Space Climate*, **3**, A02. https://doi.org/10.1051/swsc/2013025. 2, 3.2.1, 3.3, 3.3, 5.2

Mott-Smith, H. M., and I. Langmuir, 1926. The theory of collectors in gaseous discharges. *Phys. Rev.*, **28**, 727–763. https://doi.org/10.1103/PhysRev.28.727. 4.3, 4.3

Oksavik, K., 2020. The university of Bergen global navigation satellite system data collection. *DataverseNO*. https://doi.org/10.18710/AJ4S-X394. 4.2

Oksavik, K., C. van der Meeren, D. A. Lorentzen, L. J. Baddeley, and J. Moen, 2015. Scintillation and loss of signal lock from poleward moving auroral forms in the cusp ionosphere. *Journal of Geophysical Research: Space Physics*, **120**(10), 9161–9175. https://doi.org/10.1002/2015JA021528. 2, 3.3

Ossakow, S. L., and P. K. Chaturvedi, 1979. Current convective instability in the diffuse aurora. *Geophysical Research Letters*, **6**(4), 332–334. https://doi.org/10.1029/GL006i004p00332. 3.3

Ott, E., 1978. Theory of Rayleigh-Taylor bubbles in the equatorial ionosphere. *Journal of Geophysical Research: Space Physics*, **83**(A5), 2066–2070. https://doi.org/10.1029/JA083iA05p02066. 3.2.1

Oyama, S., A. Kero, C. J. Rodger, M. A. Clilverd, Y. Miyoshi, N. Partamies, E. Turunen, T. Raita, P. T. Verronen, and S. Saito, 2017. Energetic electron precipitation and auroral morphology at the substorm recovery phase. *Journal of Geophysical Research: Space Physics*, **122**(6), 6508–6527. https://doi.org/10.1002/2016JA023484. 3.1

Partamies, N., L. Juusola, E. Tanskanen, and K. Kauristie, 2013. Statistical properties of substorms during different storm and solar cycle phases. *Annales Geophysicae*, **31**(2), 349–358. https://doi.org/10.5194/angeo-31-349-2013. 3.1

Partamies, N., L. Juusola, D. Whiter, and K. Kauristie, 2015. Substorm evolution of auroral structures. *Journal of Geophysical Research. Space physics*, **120**(7), 5958–5972. https://doi.org/10.1002/2015JA021217. 3.1, 3.1

Partamies, N., K. Kauristie, T. I. Pulkkinen, and M. Brittnacher, 2001. Statistical study of auroral spirals. *Journal of Geophysical Research: Space Physics*, **106**(A8), 15,415–15,428. https://doi.org/10.1029/2000JA900172. 3.1

Partamies, N., M. Syrjäsuo, E. Donovan, M. Connors, D. Charrois, D. Knudsen, and Z. Kryzanowsky, 2010. Observations of the auroral width spectrum at kilometre-scale size. *Annales Geophysicae*, **28**(3), 711–718. https://doi.org/10.5194/angeo-28-711-2010. 3.1

Partamies, N., J. M. Weygand, and L. Juusola, 2017. Statistical study of auroral omega bands. *Annales Geophysicae*, **35**(5), 1069–1083. https://doi.org/10.5194/angeo-35-1069-2017. 3.1

Partamies, N., D. Whiter, K. Kauristie, and S. Massetti, 2022. Magnetic local time (MLT) dependence of auroral peak emission height and morphology. *Annales Geophysicae*, **40**(5), 605–618. https://doi.org/10.5194/angeo-40-605-2022. 4.1

Phan, T. D., L. M. Kistler, B. Klecker, G. Haerendel, G. Paschmann, et al., 2000. Extended magnetic reconnection at the Earth's magnetopause from detection of bi-directional jets. *Nature (London)*, **404**(6780), 848–850. https://doi.org/10.1038/35009050. 3.1

Pitout, F., and Y. V. Bogdanova, 2021. The Polar Cusp Seen by Cluster. *Journal of Geophysical Research: Space Physics*, **126**(9), e2021JA029,582. https://doi.org/10.1029/2021JA029582. 3.3

Prikryl, P., L. Spogli, P. T. Jayachandran, J. Kinrade, C. N. Mitchell, et al., 2011. Interhemispheric comparison of GPS phase scintillation at high latitudes during the magnetic-cloud-induced geomagnetic storm of 5-7 April 2010. *Annales Geophysicae*, **29**(12), 2287–2304. https://doi.org/10.5194/angeo-29-2287-2011. 5.2

Rino, C., and E. Fremouw, 1977. The angle dependence of singly scattered wavefields. *Journal of Atmospheric and Terrestrial Physics*, **39**(8), 859–868. https://doi.org/10.1016/0021-9169(77)90166-0. 3.3

Seeber, G., 2003. Satellite geodesy. De Gruyter, Berlin, New York. ISBN 9783110200089. https://doi.org/10.1515/9783110200089. 3.3

Semeter, J., S. Mrak, M. Hirsch, J. Swoboda, H. Akbari, et al., 2017. GPS signal corruption by the discrete aurora: precisemMeasurements from the Mahali experiment. *Geophysical Research Letters*, **44**(19), 9539–9546. https://doi.org/10.1002/2017GL073570. 2, 5.2

Skone, S., K. Knudsen, and M. de Jong, 2001. Limitations in GPS receiver tracking performance under ionospheric scintillation conditions. *Physics and Chemistry of the Earth Part A, Solid earth and geodesy*, **26**(6-8), 613–621. https://doi.org/10.1016/S1464-1895(01)00110-7. 3.3

Smith, A. M., C. N. Mitchell, R. J. Watson, R. W. Meggs, P. M. Kintner, K. Kauristie, and F. Honary, 2008. GPS scintillation in the high arctic associated with an auroral arc. *Space Weather*, **6**(3). https://doi.org/10.1029/2007SW000349. 2

Spicher, A., A. A. Ilyasov, W. J. Miloch, A. A. Chernyshov, L. B. N. Clausen, J. I. Moen, T. Abe, and Y. Saito, 2016. Reverse flow events and small-scale effects in the cusp ionosphere. *Journal of Geophysical Research: Space Physics*, **121**(10), 10,466–10,480. https://doi.org/10.1002/2016JA022999. 3.3

Spicher, A., W. J. Miloch, L. B. N. Clausen, and J. I. Moen, 2015. Plasma turbulence and coherent structures in the polar cap observed by the ICI-2 sounding rocket. *Journal of Geophysical Research: Space Physics*, **120**(12), 10,959–10,978. https://doi.org/10.1002/2015JA021634. 3.3

Spogli, L., C. Cesaroni, D. Di Mauro, M. Pezzopane, L. Alfonsi, et al., 2016. Formation of ionospheric irregularities over Southeast Asia during the 2015 St. Patrick's Day storm. *Journal of Geophysical Research: Space Physics*, **121**(12), 12,211–12,233. https://doi.org/10.1002/2016JA023222. 3.3, 5.2

Sreenivash, V., Y. Su, and S. Datta-Barua, 2020. Automated ionospheric scattering layer hypothesis generation for detected and classified auroral global positioning system scintillation events. *Radio Science*, **55**(1), e2018RS006,779. https://doi.org/10.1029/2018RS006779. 2

Sugiura, M., 1964. Hourly values of equatorial Dst for the IGY. *Ann. Int. Geophys. Yr.*, **35**. URL https://www.osti.gov/biblio/4554034. 3.1

Treumann, R. A., 1997. Advanced space plasma physics. Imperial College Press. ISBN 9781860940262. https://doi.org/10.1142/p020. 3.2.2, 3.2.3, 3.2.4, 3.5, 3.6, 3.2.5

Tsunoda, R. T., 1988. High-latitude F region irregularities: A review and synthesis. *Reviews of Geophysics (1985)*, **26**(4), 719–760. https://doi.org/10.1029/RG026i004p00719. 3.3, 3.3

van der Meeren, C., K. Oksavik, D. A. Lorentzen, M. T. Rietveld, and L. B. N. Clausen, 2015. Severe and localized GNSS scintillation at the poleward edge of the nightside auroral oval during intense substorm aurora. *Journal of Geophysical Research: Space Physics*. https://doi.org/10.1002/2015JA021819. 2, 3.3, 4.2, 5.2

Weber, E. J., J. Buchau, J. G. Moore, J. R. Sharber, R. C. Livingston, J. D. Winningham, and B. W. Reinisch, 1984. F layer ionization patches in the polar cap. *Journal of Geophysical Research*, **89**(A3), 1683–1694. https://doi.org/10.1029/JA089iA03p01683. 3.2.1

Weber, E. J., R. T. Tsunoda, J. Buchau, R. E. Sheehan, D. J. Strickland, W. Whiting, and J. G. Moore, 1985. Coordinated measurements of auroral zone plasma enhancements. *Journal of Geophysical Research: Space Physics*, **90**(A7), 6497–6513. https://doi.org/10.1029/JA090iA07p06497.1. 5.2

Whiter, D. K., N. Partamies, B. Gustavsson, and K. Kauristie, 2023. The altitude of green OI 557.7 nm and blue N_2^+ 427.8 nm aurora. *Annales Geophysicae*, **41**(1), 1–12. 10.5194/angeo-41-1-2023, URL https://angeo.copernicus.org/articles/41/1/2023/. 4.1

Yeh, K. C., and C.-H. Liu, 1982. Radio wave scintillations in the ionosphere. *Proceedings of the IEEE*, **70**(4), 324–360. https://doi.org/10.1109/PROC.1982.12313. 3.3

Zheng, Yuhao, Xiong, Chao, Jin, Yaqi, Liu, Dun, Oksavik, Kjellmar, et al., 2022. The refractive and diffractive contributions to GPS signal scintillation at high latitudes during the geomagnetic storm on 7-8 September 2017. *J. Space Weather Space Clim.*, **12**, 40. https://doi.org/10.1051/swsc/2022036. 3.3, 3.3

Papers

Paper I

Ionospheric Plasma Structuring in Relation to Auroral Particle Precipitation

Florine Enengl, Daria Kotova, Yaqi Jin, Lasse B.N. Clausen, Wojciech J. Miloch

Published in *Journal of Space Weather and Space Climate*, 2023, volume 13, issue 1, DOI: 10.1051/swsc/2022038.

J. Space Weather Space Clim. 2023, **13**, 1
© F. Enengl et al., Published by EDP Sciences 2023
https://doi.org/10.1051/swsc/2022038

Available online at:
www.swsc-journal.org

Topical Issue - Ionospheric plasma irregularities and their impact on radio systems

RESEARCH ARTICLE **OPEN ACCESS**

Ionospheric plasma structuring in relation to auroral particle precipitation

Florine Enengl[*], Daria Kotova, Yaqi Jin, Lasse B.N. Clausen, and Wojciech J. Miloch

Department of Physics, University of Oslo, Problemveien 7, 0315 Oslo, Norway

Received 11 May 2022 / Accepted 29 November 2022

Abstract – Auroral particle precipitation potentially plays the main role in ionospheric plasma structuring. The impact of auroral particle precipitation on plasma structuring is investigated using multi-point measurements from scintillation receivers and all-sky cameras from Longyearbyen, Ny-Ålesund, and Hornsund on Svalbard. This provides us with the unique possibility of studying the spatial and temporal dynamics of the aurora. Here we consider three case studies to investigate how plasma structuring is related to different auroral forms. We demonstrate that plasma structuring impacting the GNSS signals is largest at the edges of auroral forms. Here we studied two stable arcs, two dynamic auroral bands, and a spiral. Specifically for arcs, we find elevated phase scintillation index values at the poleward edge of the aurora. This is observed for auroral oxygen emissions (557.7 nm) at 150 km in the ionospheric E-region. This altitude is also used as the ionospheric piercing point for the GNSS signals as the observations remain the same regardless of different satellite elevations and azimuths. Further, there may be a time delay between the temporal evolution of aurora (e.g., commencement and fading of auroral activity) and observations of elevated phase scintillation index values. The time delay could be explained by the intense influx of particles, which increases the plasma density and causes recombination to carry on longer, which may lead to a persistence of structures – a "memory effect". High values of phase scintillation index values can be observed even shortly after strong visible aurora and can then remain significant at low intensities of the aurora.

Keywords: Particle precipitation / Phase Scintillation Index / Auroral plasma structuring / Ionospheric E-region

1 Introduction

The aurora can be seen as the signature of direct coupling between the ionosphere and magnetosphere. During the high geomagnetic activity, energetic particle precipitation leads to higher intensity of the aurora resulting in different auroral forms. Dynamical processes in the E- and F-regions of the ionosphere are often associated with instabilities and turbulence which result in plasma structuring and irregularities at various scales. Such irregularities in ionospheric plasma density have an impact on the propagation of radio waves (e.g., Keskinen & Ossakow, 1983; Huba et al., 1985; Kintner & Seyler, 1985; Moen et al., 2013; Deshpande et al., 2014). Trans-ionospheric radio waves propagating through regions with density irregularities undergo diffraction and refraction, and they result in rapid fluctuations in phase and amplitude of the received signal, referred to as scintillation (e.g., Hey et al., 1946; Kintner et al., 2007). Scintillation of the received signal affects man-made systems, such as radio communication and/or satellite-based positioning systems. At the same time, scintillation of the received signal can be used as an indication for ionospheric plasma structuring. This will be also the approach in this work, where we will focus on the role of the auroral particle precipitation during geomagnetic substorms and investigate how different discrete auroral forms, i.e., stable arcs and fast-moving forms (such as spirals), relate spatially and temporally to structuring in the ionospheric plasma density.

The Earth's ionosphere and magnetosphere are directly coupled in the polar regions via the Birkeland currents, which can be seen as drivers for the aurora. There is a variety of resulting auroral forms, which have been categorized over many years with regard to their shapes, process, and lifetime, but to this day there is no clear and well-accepted definition for all of the forms. Some auroral forms and their evolution can be linked to certain substorm phases (e.g., Akasofu, 1966; Elphinstone et al., 1996; Partamies et al., 2015). The auroral arcs are well-studied phenomena in quiet (for a review see Karlsson et al., 2020) and active geomagnetic periods. Davis (1978) studied auroral arcs and their distortions into complex forms (spirals and curls) and defined an auroral arc as a recognizable luminosity resulting from the impingement of a field-aligned sheet beam of charged particles upon the atmosphere. The most simple form is an east-west elongated quiet discrete

---

[*] Corresponding author: `florine.enengl@fys.uio.no`

auroral arc. The width of the arc can be very thin (0.5–1.5 km) (Partamies et al., 2010), but most mesoscale-size arcs have an observed width of around 10–50 km (Knudsen et al., 2001).

Arcs often appear in multiple-arc structures and are found both during quiet and active periods. Multiple arc structures are arrays of arcs that are near-parallel to each other and in close proximity, and they are also the most common form of discrete auroral observations (Davis, 1978; Gillies et al., 2014). The multiple arc structures are referred to as arc packets when they are formed by splitting the trailing arc into two, possibly due to the Alfvén wave dispersion (Semeter et al., 2009). Stable and quiet auroral arcs are expected in the evening and at nighttime. Here, we will study auroral emissions in the night time sector from 21:00 to 03:00 MLT (magnetic local time).

Other notable auroral distortions are curl, spiral, bands, ray forms, westward traveling surge or omega bands (e.g., Hallinan & Davis, 1970; Elphinstone et al., 1996; Ivchenko et al., 2005; Partamies et al., 2017). In this paper, we will focus on spiral structures. Spirals are larger-scale auroral vertices (20–1300 km), which form as the aurora twists counter-clockwise. It is suggested that the Kelvin-Helmholtz instability could play a role in the formation of the spiral (Hallinan & Davis, 1970; Davis & Hallinan, 1976; Hallinan, 1976; Partamies et al., 2001). While Davis and Hallinan (1976) and Keiling et al. (2009) relate spirals to magnetically disturbed periods, Partamies et al. (2001) relate them primarily to magnetically quiet conditions. However, fast-moving spirals, whose signatures are only found in a single all-sky camera (ASC) image, seem to be related to increasing geomagnetic activity Partamies et al. (2001).

A variety of highly dynamic phenomena (e.g., polar cap patches, field-aligned currents, high-density F-region plasma, or particle precipitation) cause plasma irregularities in the E- and F-regions ionosphere (e.g., Moen et al., 2013; van der Meeren et al., 2015; Jin et al., 2016, 2017; Spogli et al., 2016; Fæhn Follestad et al., 2020). Ionospheric plasma structuring can be indirectly observed by scintillation receivers. Recorded signals allow for calculating the phase and amplitude scintillation index values. At high latitudes, the effect of irregularities on the trans-ionospheric wave can also be reflected in the degradation of the receiver tracking performance, Total Electron Content (TEC) jumps, and cycle slips (Skone et al., 2001; Alfonsi et al., 2008; Moen et al., 2013; Chernyshov et al., 2020; references therein).

Auroral particle precipitation can lead to significant plasma irregularities (Kelley et al., 1982; Keskinen & Ossakow, 1983; Weber et al., 1985; Prikryl et al., 2011), but it is still an open question to what extent it contributes to plasma structuring and whether it is dominant in the E or F-region ionosphere. It is observed that soft particle precipitation is unlikely to be the main source of the large-scale F-region plasma structures on the nightside (Jin et al., 2016). While on the dayside the main ionization source of the E-region is the EUV solar radiation, on the nightside Joule heating and auroral particles with energies of 10–30 keV dominate the energy input into the system (Millward et al., 1999; Wilson et al., 2006; Nikolaeva et al., 2021).

There have been previous studies that tried to answer this question. Kinrade et al. (2013) studied ionospheric irregularities caused by the auroral particle precipitation using scintillation receivers and auroral imagers located at the South Pole. They found spatially and temporally well-correlated scintillations with atomic oxygen emissions at wavelengths of λ = 557.7 nm and 630.0 nm. This correlation is better for emissions at λ = 557.7 nm, which could be due to the tracking method's effectiveness at two emission wavelengths of different characteristic intensities. They found optical images of aurorae to be a useful spatial and temporal indicator of the GPS phase scintillations during intense and persistent auroral activity, especially for discrete arcs and at the auroral boundary. Another study, by van der Meeren et al. (2015), sheds light on the Global Navigation Satellite System's (GNSS's) signal scintillations during intense substorm aurora. The data was recorded at GNSS receivers around Svalbard. They observed severe phase scintillation, which was following the intense poleward edge of the auroral oval as it expanded poleward and showed that received signals may experience strong scintillation when they intersect oxygen (λ = 557.7 nm) emissions. The satellite systems of GPS, GLONASS, and Galileo were affected similarly through the scintillations in relation to the intense line of sight auroral emissions in a highly localized region of the sky. Discrete aurora and GPS signal corruption have been studied by Semeter et al. (2017), using a network of receivers and imagers in Alaska. The ASC sampled images of oxygen emissions at λ = 558 nm. The auroral form of interest was a westward traveling surge and the loss of lock events consistently appeared at the edges of auroral forms. The scintillation regions were confined to a narrow strip (<20 km) tangential to the trailing edge of the observed aurora. As the appearance of the loss of lock events consistently followed the auroral boundaries irrespective of the satellite elevation and azimuth, the authors suggested the source to be near the oxygen 558 nm emission line. This is within the E-region of the ionosphere. A consequent study from Mrak et al. (2018), using co-located GPS-ASI sensors in Alaska to remove mapping ambiguity, concludes that E-region electrodynamic processes are sources of plasma irregularities.

The following two questions remain open: i) in which layer of the ionosphere does the auroral particle precipitation play a dominant role in plasma structuring? ii) what spatial and temporal characteristics of the enhanced scintillation index values relate to which auroral forms? In this paper, we will study how stable auroral arcs and fast-moving forms (bands and spirals) relate spatially and temporally to ionospheric plasma structuring. The observations are made by using several scintillation receivers and ASCs located in Longyearbyen, Ny-Ålesund, and Hornsund on Svalbard. Case studies that consider different auroral forms during the substorm events are presented. We observe elevated values of the phase scintillation index poleward of the arcs, and at the boundaries of fast-moving forms. These characteristics have been found for the 557.7 nm oxygen emissions, indicating that the auroral particle precipitation in the E-region can contribute to relevant plasma structuring. We also observe a short time delay between the onset of the aurora and observed plasma structuring.

2 Instruments and approach

To study whether plasma structuring is driven by particle precipitation, we investigate the relative location between elevated scintillation index values and the aurorae. For this purpose, we use data from three ASC on Svalbard. Two of the cameras are Keo Sentry 4ix Monochromatic Imagers from

KEO Scientific, with filters, operated by the University of Oslo (UiO). They are situated in Longyearbyen (LYR, geographic coordinates: 78.15° N, 16.04° E), and in Ny-Ålesund (NYA, geographic coordinates 78.92° N, 11.93° E). The imagers record emission intensities every 30 s, with a field of view (FOV) of 180°. Both imagers are equipped with narrowband filters to monitor 557.7 nm (green) and 630.0 nm (red) auroral emissions. For the analysis, the ASC images are projected to 150 km and 250 km (green and red auroral emission altitudes) respectively. The imager in Hornsund (HOR, geographic coordinates 77° N, 15.55° E) is a Sony A7 SII color camera with a FOV of 180, also operated by UiO. The availability of recorded images for this camera on the days of interest is every 15 min. The ASCs are used to determine the form of the aurora and its relative location to the observed elevated scintillation index values of Global Navigation Satellite Systems (GNSS) signals.

To analyze the impact of auroral particle precipitation on the GNSS signals, five GNSS ionospheric scintillation receivers on Svalbard are used in this study. The delay Δt of a signal propagating through a plasma is dependent on the electron density n_e and the signal frequency f:

$$\Delta t = \frac{40.3}{cf^2} \int n_e \mathrm{d}\rho, \tag{1}$$

with c being the speed of light, ρ the ray path (e.g., Kintner et al., 2005, 2007).

The phase ϕ is connected to time delay Δt and therefore to electron density variations along the signal path (Eq. (1)) through

$$\phi = f\Delta t, \tag{2}$$

(e.g., Yeh & Liu, 1982; Kintner et al., 2007). As the phase is affected by the time delay and electron content variations it indicates plasma structuring processes. Phase fluctuations are caused by irregularities covering the full range of scales from meters to a few kilometers (e.g., Basu et al., 1998; Kintner et al., 2007). The phase scintillation index σ_ϕ,

$$\sigma_\phi = \langle \phi^2 \rangle - \langle \phi \rangle^2, \tag{3}$$

is the standard deviation of the detrended measured phase and is dominated by large-scale fluctuations (Yeh & Liu, 1982; Kintner et al., 2007). Even though the index is not issue-free, for example, due to the dominance of the low-frequency component of the phase power spectrum, the phase or related electron density variations nevertheless can indicate physical structuring in the ionosphere (Beach, 2006). Refractive and diffractive variations of σ_ϕ are not differentiated in this study, as we use σ_ϕ as a measure of plasma structuring and to study the relative location to auroral forms, but are not studying the effects on the carrier phase. Amplitude scintillations are described by the amplitude scintillation index S_4:

$$S_4 = \sqrt{\frac{\langle I^2 \rangle - \langle I \rangle^2}{\langle I \rangle^2}}, \tag{4}$$

with I being the signal intensity (e.g., Briggs & Parkin, 1963; Yeh & Liu, 1982). The S_4 index describes and is affected by irregularities in a range of hundreds of meters to meters (at and below the Fresnel radius) (e.g., Basu et al., 1998; Kintner et al., 2007).

In this study, we use the calibrated 60-second reduced data (Oksavik, 2020a) of the phase (σ_ϕ) and amplitude (S_4) scintillation index. A cut-off angle of 15° is applied to the scintillation data to minimize multipath effects.

The data is recorded by NovAtel GPStation-6 receivers. The receiver in Hornsund is situated about 500 m from the ASC and is run by the University of Oslo. The receivers situated in Ny-Ålesund (co-located with the NYA ASC), Longyearbyen (co-located with the LYR ASC), Bjørnøya (BJN, geographic coordinates 74.50° N, 19° E), and Hopen (HOP, geographic coordinates 76.51° N, 25.01° E) are operated by the University of Bergen (Oksavik, 2020b). The receivers track GPS, Galileo, and GLONASS satellites. We use all received signals (GPS: L1CA, L2Y, L2C, L2P, L5Q; GLONASS: L1CA, L2CA, L2P; GALILEO: E1, E5A, E5B, E6) as they have previously been shown to be similarly affected by ionospheric irregularities (van der Meeren et al., 2015; Alfonsi et al., 2016).

The Interplanetary Magnetic Field (IMF) data and the solar wind conditions are downloaded from NASA/GSFC's OMNI data set through OMNIWeb (King & Papitashvili, 2005). We assess the IMF Bz magnetic field component, the solar wind flow speed, and sym-H (1-min resolution GSM (geocentric solar magnetospheric coordinates) data). A negative IMF Bz component can indicate dayside reconnection. The sym-H index is a measure of the magnetospheric ring current intensity and is used to quantify geomagnetic storms. The index is calculated using data from different magnetometer stations near the equator and describes the symmetric part of the magnetic field horizontal component (Wanliss & Showalter, 2006). These indices help to describe and filter for background conditions and evaluate whether the geomagnetic conditions indicate geomagnetic storms. To investigate substorm conditions the horizontal component of the local magnetic field was used. It is recorded by a magnetometer network around Svalbard operated by the Tromsø Geophysical Observatory (Tanskanen, 2009). The decrease in the B_x component of the magnetic field at high latitudes is a signature of the enhancement of the westward electrojet and the substorm current wedge in superposition with eastward electrojet enhancements (Akasofu, 1965; D'Onofrio et al., 2014). Further, we use the Kp index (from GFZ Potsdam and the National Geophysical Data Center), which is a proxy for the energy input from the solar wind to the magnetosphere. The Kp index is calculated based on 13 selected subauroral ground-based magnetic observatories and is the mean value of the disturbance levels in the horizontal magnetic field components. Higher Kp values correspond to stronger disturbances (Matzka et al., 2021).

3 Case selection and conditions

Data from the ASC network were used to select events for the case study. The first season (2019/2020) when all three cameras (NYA, LYR, HOR) were in operation and recorded data, is considered for this study. The season spans from October-March. On 73 days all three ASCs have recorded data in an overlapping timespan (2 h). Days with Kp < 5 were excluded. This reduced the set to 24 days. The solar wind conditions for each of the selected events are shown in Figure 1. Most of these days are part of six longer lasting multi-day (5+ days) moderate geomagnetic storm events with high solar wind

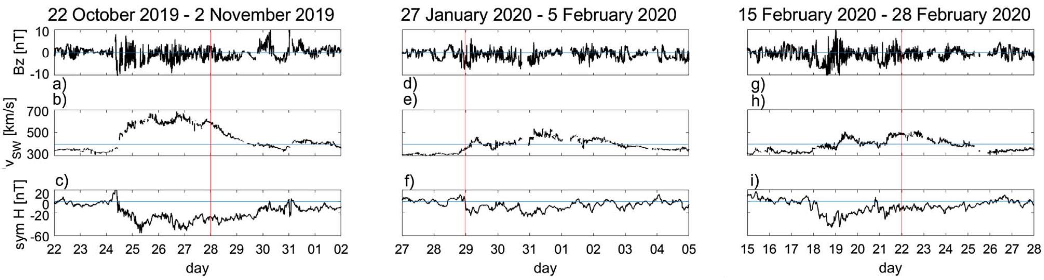

Fig. 1. Solar wind data recorded during the selected case study dates: 28 October 2019 (a–c), 29 January 2020 (d–f), and 22 February 2020 (g–i), indicated by red vertical lines. Panels a, d, and g show the solar wind/interplanetary magnetic field Bz component, indicating reconnection with Earth's magnetic field when negative. Panels b, e, and h show the solar wind flow speed that during geomagnetic storms increases to over 400 km/s, as indicated by a horizontal line, while the sym-H component (a measure of the ring current), shown in panels c, f, and i abruptly goes negative during storms with a change of sym $H > 20$ nT (here the horizontal line corresponds to zero).

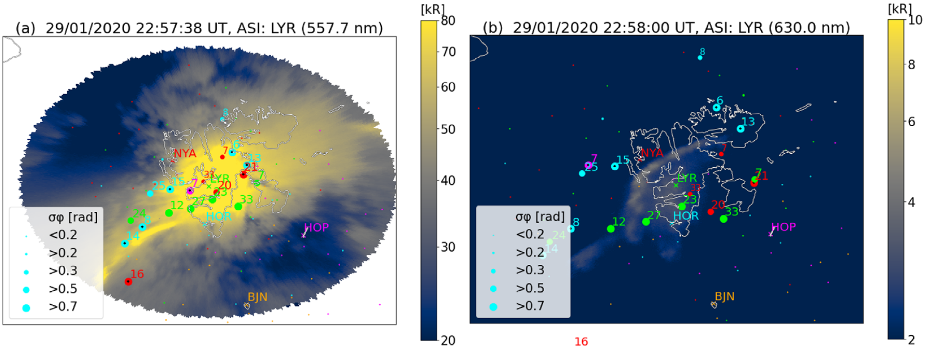

Fig. 2. The projection of the 557.7 nm (panel a)/630.0 nm (panel b) emissions shown together with the phase scintillation index σ_ϕ over a map of Svalbard on 29 January 2020 as seen from the LYR ASC. Brighter yellow auroral emissions mean stronger intensity and bigger markers mean stronger σ_ϕ. The markers represent σ_ϕ measurements from NYA in red, LYR in green, HOR in cyan, HOP in magenta, and BJN in orange. While the elevated σ_ϕ follow the shape of the 557.7 nm auroral emissions shown in panel a, they are observed displaced with regards to the 630.0 nm auroral emissions shown in panel b.

speeds (above 400 km/s; see Figs. 1b, 1e, 1h), negative sym-H component (−20 nT to −40 nT; see Figs. 1c, 1f, 1i), re-occurring negative Bz (see Figs. 1a, 1d, 1g) and negative drops of the local B_x component (shown in Figs. 3a, 3e, 3i). For comparability of the cases events with available data between 18:00 and 20:00 UT (21:00–03:00 MLT nightside) were selected, which means the data set has been reduced to find times at which all three ASC recorded continuous data in the majority of the 18:00–24:00 UT section. The set is now down-filtered to 12 days as the remaining candidates for the case study. After the filtering process, the imagery was visually assessed and out of the days with intense auroral emissions, the days with the least cloud cover (for all three ASC) that were part of different geomagnetic storm events were selected. The selected dates are 28 October 2019, 29 January 2020, and 22 February 2020. The similarity in the events lies in the background conditions as all selected dates are substorm events with Kp > 5. The events are in the night sector to meet similar geomagnetic conditions and types of aurora. Particle precipitation is strongly visible on all of them. The randomness in the case study events is achieved through limited data availability and cloud cover on the ASC images, providing us with a representative set of case studies with similar conditions, but spread over the whole season.

4 Observations

Figure 3 shows data from the selected case study dates: 28 October 2019, 29 January 2020, and 22 February 2020 from 18:00 to 24:00 UT. In Figures 3a, 3e, and 3i the horizontal magnetic field component B_x is shown. The decreases in B_x indicate substorm events at the respective stations (NYA-red, LYR-green, HOP-black, BJN-orange, HOR-blue). Times of intense particle precipitation can be investigated by presenting the center pixel column of the ASC images as a time series – this time versus latitude plot is named a keogram. The keograms reveal times of auroral activity above the zenith of the recording ASC. The keograms presented in Figures 3b, 3f, and 3j show images that originate from the LYR ASC using the filter for

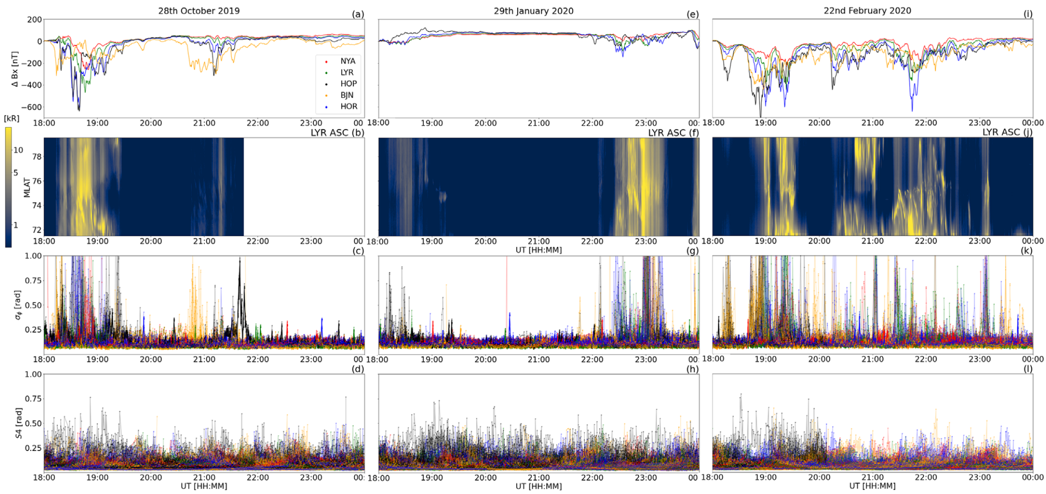

Fig. 3. Data from the selected events: 28 October 2019, 29 January 2020, and 22 February 2020 from 18:00 to 24:00 UT. In panels a, e, and i, the horizontal magnetic field component B_x is shown. The dips indicate substorm events at the respective stations (NYA – red, LYR – green, HOP – black, BJN – orange, HOR – blue). Panels b, f, and j show the 557.7 nm emissions intensity observed by the LYR ASC in form of a keogram. The bright auroral emissions correspond to times of particle precipitation. Panels c, g, k and d, h, l show σ_ϕ and S_4 scintillation index data recorded by the scintillation receivers in the respective stations. They quantify the location, scale, and intensity of plasma structuring.

557.7 nm (green) emissions. Here we associate the auroral activity, visible bright auroral emissions, with times of particle precipitation. Figures 3c, 3g, 3k and 3d, 3h, 3l show σ_ϕ and S_4 scintillation index data recorded by the scintillation receivers in the respective stations. The indices are used to quantify plasma structuring in location, intensity, and scale. The S_4-index indicates plasma structuring on scales down to a few meters, below the Fresnel radius, while σ_ϕ indicates structuring above the Fresnel radius (hundreds of meters to km).

4.1 Altitude of plasma structuring

Different regions in the ionosphere are influenced by different phenomena characteristic of the specific altitude ranges. Determining the altitude which the GNSS signals are disrupted is crucial to relate the disturbances observed through the phase scintillation index to physical phenomena. To answer in which layer of the ionosphere the auroral particle precipitation plays a dominant role in plasma structuring, we evaluate whether elevated σ_ϕ corresponds better to red or green auroral emissions and at what mapping altitude the auroral evolution corresponds best to elevated σ_ϕ. In order to do so, we first establish whether the elevated σ_ϕ corresponds to aurorae and if so to which wavelength (Step 1). Then we discuss the mapping ambiguity and why we can project all data (ASC and scintillation receivers) to the same altitude (Step 2).

Step 1: The images of green and red auroral emissions are projected to their estimated emission altitudes (150 km and 250 km respectively). The scintillation index values are projected to different altitudes (piercing points) to find out whether the observed disturbances happen in the same altitude range as the auroral emissions and whether they correspond better to the green or red emissions. For this, different piercing points between 100 km to 350 km were tested, while the auroral emission projections were kept constant at their respective estimated altitudes. For the green auroral emissions (150 km), it is observed that for lower (100 km) or higher (200 km) piercing point altitudes, the elevated σ_ϕ values appear randomly placed with regards to the auroral forms. When observing small patches of auroral emissions further east/west of zenith, one observes the elevated σ_ϕ values further east/west of the patch when the ionospheric piercing point is chosen low/high. However, when choosing the green auroral emission altitude as the altitude of the piercing points, we find that the elevated σ_ϕ values occur at the boundaries and align well with the evolution of auroral forms. Using imagery from all three ASC and all five receivers, elevated σ_ϕ values are consistently found at the edges of the auroral forms for this piercing point altitude. This indicates that the signal is impacted right at the altitude of green auroral emission. This pattern has not been detected to the same extent with regards to red auroral emissions, see an example in Figure 2 and Videos (S1 – green emissions; S2 – red emissions) in the supplementary material.

This behavior is observed for chosen piercing points for satellites regardless of satellite azimuth or elevation, just as in Semeter et al. (2017). The elevated σ_ϕ values are increased at the boundaries of the auroral emissions, invariant with different satellite elevations. However, as we do not use the magnetic field inclination or orientation, this is not our main reason for allowing the projection of all data from different receivers to the same altitude.

Step 2: Better evidence to use the green auroral emission altitude as a piercing point for all our receivers is given when projecting data of only the co-located imager and scintillation receiver on the same plot, a case where the mapping altitude is irrelevant. We again observe elevated σ_ϕ values primarily at the poleward edges of the aurora, as can be seen in the video using data from only the NYA ASC and NYA scintillation receiver in the supplementary material (Video S3). Now, let us consider the case in which we project scintillation receiver data from different stations onto the same NYA ASC image. When we use, e.g., 120 km as a piercing point and projection plane for the ASC instead of 150 km, we find only very minor off-sets in relation to the auroral forms, which do not change our conclusions. As the aurorae are observed in the south of Svalbard and the ASCs, satellite positions are shown slightly further north when the piercing point and ASC projection are adjusted to a lower altitude. With this regard, mapping to an even lower altitude would only strengthen our conclusions of observing poleward elevated σ_ϕ. Note that in step 1 we vary the projections of the aurorae with the piercing point altitude, to understand how sensitive our results are when mapping all our data to different altitudes within the E-region. Whereas in step 2 we vary only the piercing point while keeping the ASC images projected to 150 km, to find whether the structuring processes happen at the same altitude as green auroral emissions.

The emission altitude of green auroral emissions is used as the piercing point altitude for the study along with ASC images of the green auroral emissions.

4.2 Case studies: spatial and temporal evolution of plasma structuring

ASC imagery of the three case study events are shown in this section. The ASC images (green aurora projected to 150 km) are plotted onto the geographical coordinates and a map of Svalbard is shown in contrast. On top of that, the observed phase scintillation data (piercing point 150 km) is displayed. The phase scintillation data is referred to as slightly elevated σ_ϕ above 0.2 rad, moderately elevated σ_ϕ above 0.3 rad, strongly elevated σ_ϕ above 0.5 rad, and very strongly elevated σ_ϕ above 0.7 rad. Not all of the measured data during, auroral activity of that day is shown: very faint aurora, forms that are not classified as part of a process showing arcs/spirals/bands, the forms that are mostly cut off by the FOV or repetitive images are excluded. The auroral activity is fluctuating in intensity and can decrease to low-intensity values or vanish shortly from the observation location before it onsets again. Whether low-intensity aurora or no aurora is observed is difficult to distinguish, as it depends on the chosen intensity scale of what will be visible. In the following, intensities measured under 10 kR-NYA/20 kR-LYR are referred to as no visible aurora. This threshold has been chosen as the elevated phase scintillation index is not observed in combination with intensities under 10 kR for NYA and 20 kR for LYR before the auroral onset. It can however be observed after the aurora vanished, this may have other reasons than auroral emissions below 10 kR/20 kR as discussed later. Only the representative images are shown in the results, but the remaining images were combined with the videos attached in the Supplementary material. Video material is available from all events as viewed from the NYA ASC and LYR ASC. The data from 22 February 2020 is also presented in form of a video recorded by the HOR ASC. In the following especially the high-intensity values of the aurora may be influenced by the way, the camera and brightness are calibrated and calculated. They are however a good measure for comparison between aurora and the σ_ϕ indices.

4.2.1 28 October 2019

The first selected event of this season occurred on 28 October 2019 (see Figs. 3a–3d). The local magnetic field B_x component shows a decrease between 18:10 and 19:30 UT measured at NYA (shown in red), LYR (green), HOP (black), BJN (orange), HOR (blue) and indicating a substorm. At HOP the magnitude of the decrease is especially large, up to a change of −600 nT in the B_x component, followed by HOR and LYR. A less severe decrease in the B_x component is observed around 20:40–21:40 UT (strongest in BJN and HOP, lightest in LYR and NYA). At the same time, the auroral activity is observed with the LYR ASC. Intense precipitation lasts from 18:15 to 19:30 UT and light precipitation from 20:45 to 21:20 UT. The latter shows only faint aurora, which is also reflected in the B_x component measurements, where we observed only light variations for LYR. Elevated σ_ϕ coincides with particle precipitation between 18:15 and 19:30 UT, this is observed for all stations. The later time interval or particle precipitation is likewise accompanied by elevated σ_ϕ, but disturbances are not in all stations recorded. BJN (Fig. 3c, shown in orange) records elevated σ_ϕ about 25 min before the strongest emissions are observed at LYR (Fig. 3b), but σ_ϕ increases right as the B_x component at BJN drops. The response of S_4 to the particle precipitation is not as clear as for σ_ϕ, but a slight increase of S_4 especially in the measurements at HOP (Fig. 3a, shown in black) may be observed around 19:00 UT. Elevated S_4 values can be an indication of diffractive effects (Yeh & Liu, 1982), but are not discussed here.

The observations on 28 October 2019 indicate a substorm event, auroral emissions, and disturbances in the phase scintillation index between around 18:10–19:30 UT and 20:40–21:40 UT (Fig. 3). This long and intense auroral activity can be best viewed from the NYA ASC as shown in Figure 4. Figures 4a–4h show a time evolution from when the auroral activity commences to when it fades out. This arc is also observed from the HOR ASC and LYR ASC. Videos of the arc from the NYA and LYR station are shown in the supplementary material (Videos S4 and S5). In Figure 4a at 18:29:23 UT light auroral activity (<30 kR) starts in the southeast quarter of the ASC's FOV, no elevation of σ_ϕ is observed at this stage. A minute later, at 18:30:23 UT, the auroral activity is at double its intensity (>60 kR) forming a faint arc. No elevation of σ_ϕ values is yet measured. At 18:31:23 UT the auroral intensity is reaching its intensity maximum (>80 kR) and now very strongly elevated σ_ϕ values are observed in the east. The delay between auroral emissions until elevated σ_ϕ values are observed is in this case 2 min, observed in LYR and NYA. The underlying processes causing elevated σ_ϕ values/plasma structuring may come with a time delay related to the recombination rates of the precipitating electrons arriving in the E-region ionosphere. The fast flows of the injected electrons could drive a two-stream instability. The difference in drift velocity between the electrons and ions, which collide with neutrals, could in specific drive the modified two-stream instability, the Farley-Buneman instability (Farley Jr., 1963). Shortly after, at 18:31:38 UT, very strongly elevated σ_ϕ values measured poleward of the established auroral arc (with an intensity still over >80 kR) are observed. Instabilities working specifically at the boundary of the particle stream may be dominant at this point, leading to very localized elevated σ_ϕ values along the poleward boundary. The intensity fluctuates

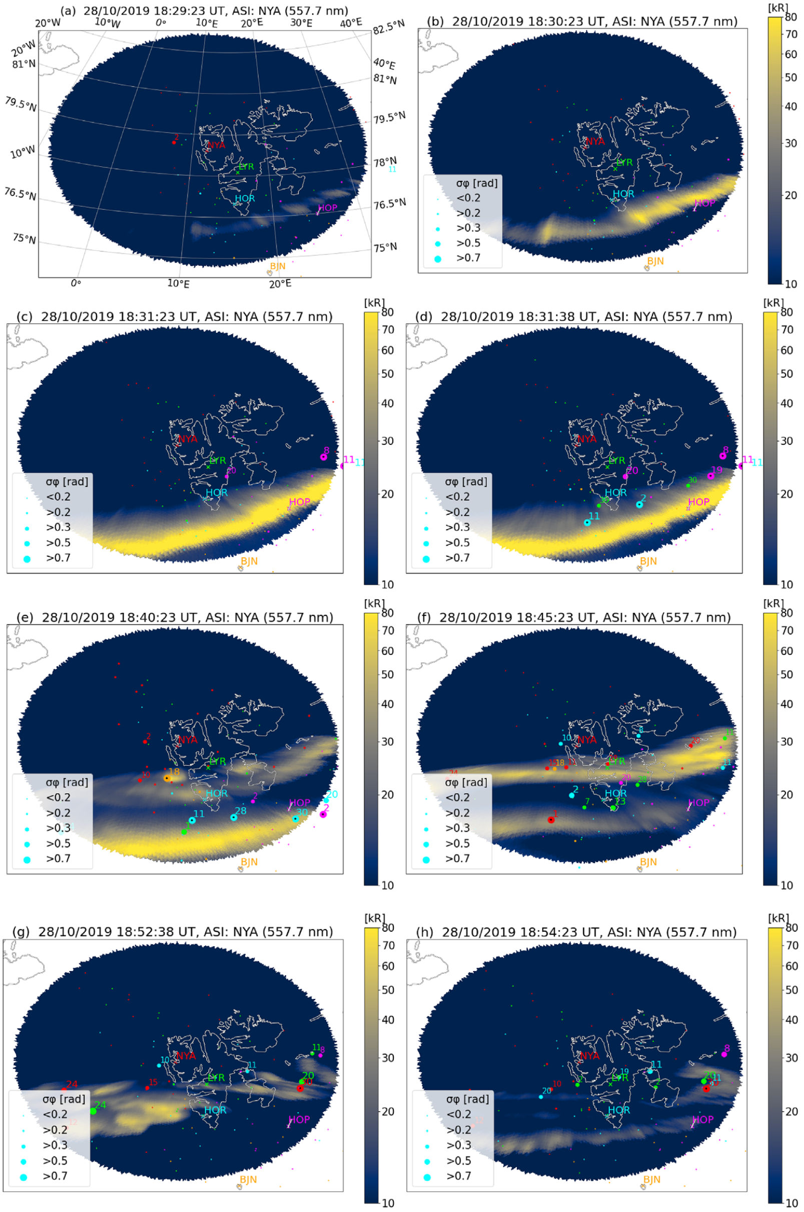

Fig. 4. The aurora shown in this figure is classified as arcs. The projection of the 557.7 nm emissions shown together with the phase scintillation index σ_ϕ over a map of Svalbard and geographical longitude/latitude on 28 October 2019 as seen from the NYA ASC for different time instances. Brighter yellow auroral emissions mean stronger intensity and bigger markers mean stronger σ_ϕ. The markers represent σ_ϕ measurements from NYA in red, LYR in green, HOR in cyan, HOP in magenta, and BJN in orange. In panel a geographic latitude and longitude gridlines are shown. The auroral intensity bar of the panel a (not shown) is the same as for the other panels in this figure. Panels a and b show the commencement of an auroral arc. Panels c and d show the arc at its maximum intensity (>80 kR). In panel d we can point out the very strongly elevated σ_ϕ poleward of the arc. Panels e and f show two auroral arcs and corresponding σ_ϕ values. Panels g and h show fading of the aurora and decrease in σ_ϕ. Even though panels a and h show similar auroral intensities (<30 kR) they show different levels of σ_ϕ: panel a – no elevated σ_ϕ, panel h – different levels of elevated σ_ϕ.

(down to <60 kR), but the σ_ϕ values stay elevated over the next 9 min. At 18:40:23 UT a second arc (with an intensity <40 kR) forms in the center of the ASC image combined with very strongly elevated σ_ϕ. The southern arc is still very intense (>80 kR) with poleward σ_ϕ values very strongly elevated. At 18:45:23 UT the arc in the center intensifies (>60 kR) and moderately elevated σ_ϕ values are observed poleward of the central arc and stronger elevated σ_ϕ values between the arcs. The southern arc has faded out (with an intensity <45 kR). At 18:52:38 UT the arc structure is dissolved and the intensity is decreased to similar values (<60 kR) as at 18:30:23 UT (before we observed elevated σ_ϕ). Occasional very strong σ_ϕ values are still observed alongside strong and moderate σ_ϕ values. This could be due to a "memory effect": the precipitation has moved away, but the E-region ionosphere has not yet restored its original state and electrons may still recombine and structures persist until the number of excess particles has declined. At 18:54:23 UT, the intensity (<30 kR) has decreased to its starting values (Fig. 4a). However occasional moderately to strongly elevated σ_ϕ values are measured. Eastwards, a low-intensity auroral patch is co-located with a very strongly elevated σ_ϕ value. The E-region ionosphere is still unstable as the structuring process continues even for weak auroral emissions.

4.3 29 January 2020

On the 29 January 2020 decreases in the local B_x component and strong auroral particle precipitation combined with increases in σ_ϕ values were observed (see Figs. 3e–3h). There are minor variations in the B_x component (about 50 nT) and light precipitation between 18:00 and 19:00 UT (Fig. 3f). After 21:50 UT fluctuations in the local B_x components are observed. The dip in B_x reaches its local minimum at a change of around −200 nT at 22:20 UT, a change much weaker than in the first studied case. Nevertheless, the auroral emissions are intense, especially around 23:00 UT. The σ_ϕ values are elevated strongly in the same time frame as precipitation is observed. The S_4 index does not show as strong a correlation to particle precipitation as σ_ϕ. In Figure 5 the event is shown as observed by the LYR ASC. In the first 30 min, the auroral activity is fluctuating and moderately elevated σ_ϕ values are found for faint aurora (<45 kR). One example is shown at 22:53:08 UT where moderately elevated σ_ϕ values are measured, but the auroral emissions are beneath (<30 kR). Whether there is a time delay in this selected case between the auroral onset and the elevated σ_ϕ values or not is difficult to determine as the auroral activity does not increase monotonically here as in the case on 28 October 2019. At 22:55:53 UT the intensity increases (>80 kR) and moderately to strongly elevated σ_ϕ values located within and surrounding the auroral form are measured. A high-intensity spiral-shaped aurora (>80 kR) is observed at 22:56:38 UT with very strongly elevated σ_ϕ. A spiral-shaped aurora has previously been linked to Kelvin-Helmholtz instability (Hallinan, 1976). The strongly elevated σ_ϕ values follow the boundary of the auroral spiral neatly, just as in Figure 4d where the elevated σ_ϕ values follow the poleward boundary of the auroral arc. At 22:57:38 UT, the auroral spiral and high-intensity area have grown. We continue to observe very strongly elevated σ_ϕ values at the boundary of the form, but now also within the form. At the boundaries of the spiral form, we observe primarily elevated σ_ϕ values poleward of the form and only rarely equatorward. A minute later at 22:58:38 UT the form has shrunk and is still surrounded by very strongly elevated σ_ϕ values. Elevated σ_ϕ values continue to be observed for over 15 min after the auroral intensity decreases below 40 kR. At 23:14:23 UT the auroral intensity is beneath 30 kR and very strongly elevated σ_ϕ values are still observed. This is another indication that there may be long-lasting structuring processes after the precipitation has declined. The observations are confirmed by the NYA and HOR cameras. The images recorded by the LYR and NYA cameras for this event are attached as Videos S1 and S6 in the supplementary material.

4.4 22 February 2020

On 22 of February multiple local negative changes in B_x, auroral emissions, and elevated σ_ϕ values are measured (see Figs. 3i–3l). In this event also S_4 is elevated, mostly in the section before 20:30 UT (Fig. 3l). The forms before 20:30 UT are very turbulent and fast moving (video of data from all three imagers shown in the Supplementary material S7, S8, and S9). The data before 20:30 UT are, due to its fast and dynamic forms, not conclusive on the spatial relation between auroral forms and elevated σ_ϕ values. Here we discuss the auroral forms after 20:30 UT as viewed from the LYR ASC. In Figure 6, at 21:00:38 UT, a band has formed in the east. The band appears fast and intense (>60 kR), with immediate strongly to very strongly elevated σ_ϕ values on the northwestward boundary of the band. No time delay between the abrupt and intense auroral onset and elevated σ_ϕ values is observed. At 21:02:08 UT the intensity has reached over 80 kR and the elevated σ_ϕ values are found in the center of the band. Here, the elevated σ_ϕ values are first observed at the boundary, but the form expands and intensifies so that the elevated σ_ϕ values move into the band-shape. Note that more GNSS satellites are crossing the band/are close to the band equatorward of HOR, but none of these are experiencing elevated σ_ϕ values. Barely any ray paths from GNSS satellites are in the band's vicinity above NYA latitudes. At 21:02:28 UT the auroral band starts fading out (<70 kR) leaving very strongly elevated σ_ϕ values poleward of the band. This is another example of how elevated σ_ϕ values are still measured for faint auroral activity. A single-point very strongly elevated σ_ϕ index can still be observed until 3 min after intense aurora. Only an auroral patch (<50 kR) is still visible in the east, here shown at 21:04:53 UT. After some minutes without strong activity, a faint auroral band (<50 kR) moves into the FOV around 21:21:53 UT, not shown in Figure 6. At 21:23:23 the form has increased its intensity to over 80 kR but only a slightly elevated σ_ϕ value is observed. Over one minute later at 21:24:38 UT the high-intensity area of the aurora grows bigger and very strongly elevated σ_ϕ values are found at the boundaries, especially poleward. Here we see again, how the auroral activity grows and expands before elevated σ_ϕ values are observed. At 21:25:52 UT the form becomes more complex, still reaching over 80 kR, and strongly to very strongly elevated σ_ϕ values are measured at the boundaries and within the form. At 21:32:38 UT (7 min later) the auroral intensity has decreased (<50 kR) and only moderately to slightly elevated σ_ϕ values are observed poleward of the band-shaped aurora. In both of the cases presented here,

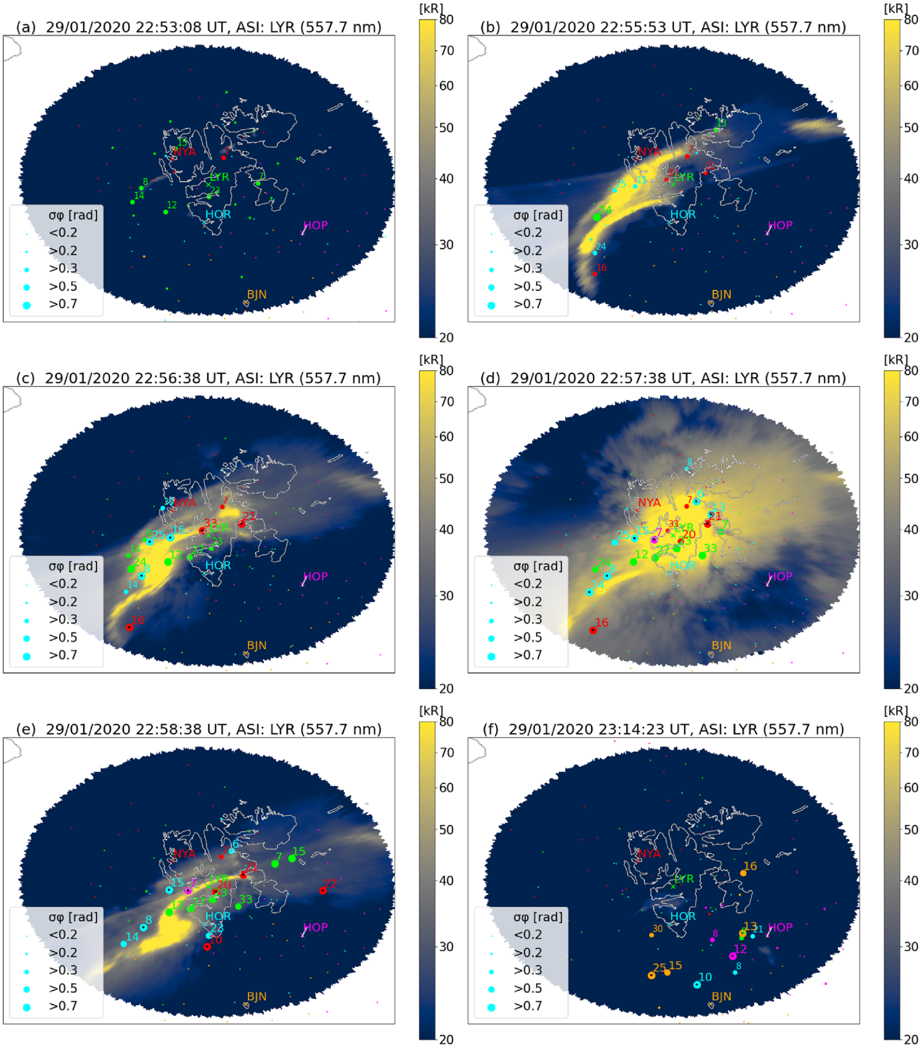

Fig. 5. The aurora shown in this figure is classified as a spiral. The projection of the 557.7 nm emissions shown together with the phase scintillation index σ_ϕ over a map of Svalbard and geographical longitude/latitude on 29 January 2020 as seen from the LYR ASC for different time instances. Brighter yellow auroral emissions mean stronger intensity and bigger markers mean stronger σ_ϕ. The markers represent σ_ϕ measurements from NYA in red, LYR in green, HOR in cyan, HOP in magenta, and BJN in orange. Panel a shows elevated σ_ϕ values yet without strong Aurora. Panel b shows strong auroral emissions and is paired with elevated σ_ϕ values. In panels c, d, and e an auroral spiral has formed and the elevated σ_ϕ values are primarily observed at the boundary of the auroral spiral. In panel f elevated σ_ϕ values on top of the faded-out form.

elevated σ_ϕ values are measured for faint aurora, suggesting plasma structuring to continue after the auroral activity has declined. On 22 February 2020 we observe fast-moving forms, and the elevated σ_ϕ values are not solely found poleward but also equatorward. As they are changing more rapidly than the other forms, the elevated σ_ϕ values may be following the auroral activity with a delay.

5 Discussion

We have studied elevated phase scintillation index values in relation to regions of auroral emission with data from three different substorm events in detail. Three distinct auroral forms were considered: arcs, spirals, and bands. While the observed arcs were stable, the other forms were more dynamic. The first

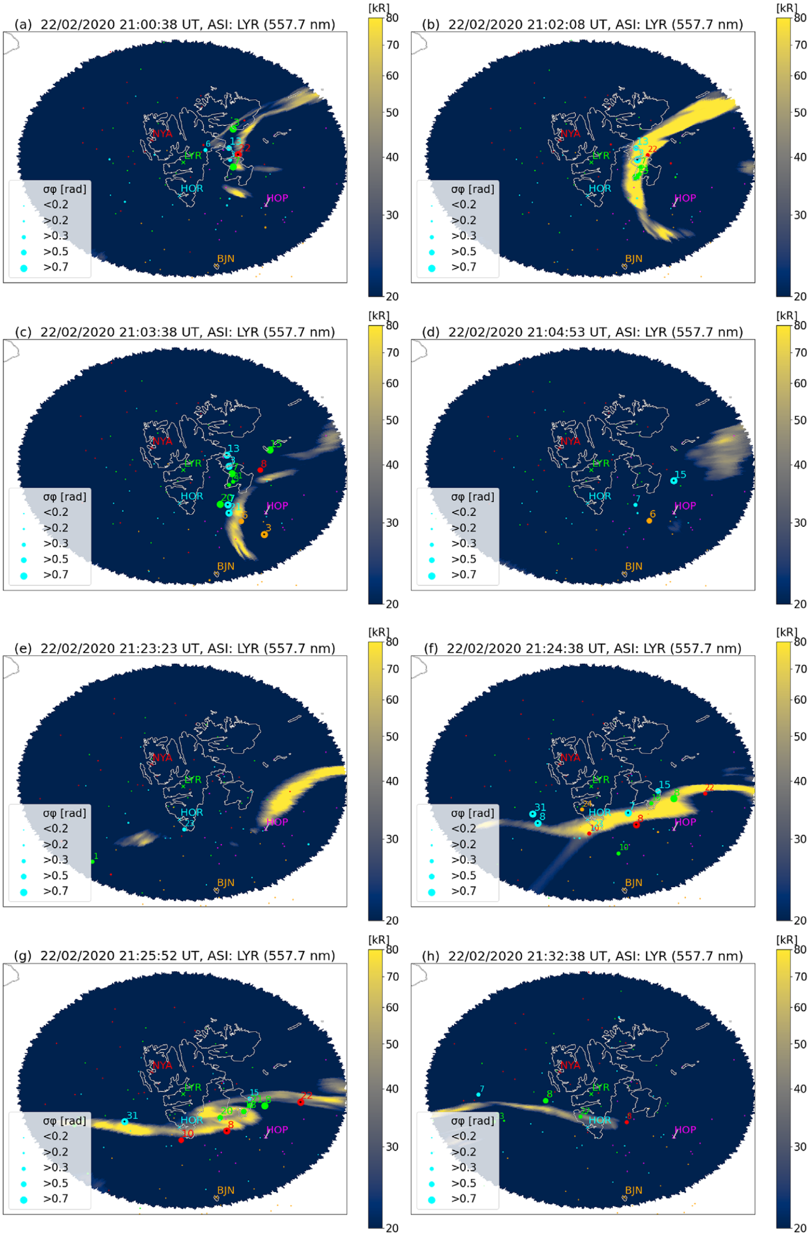
(a) 22/02/2020 21:00:38 UT, ASI: LYR (557.7 nm)

(b) 22/02/2020 21:02:08 UT, ASI: LYR (557.7 nm)

(c) 22/02/2020 21:03:38 UT, ASI: LYR (557.7 nm)

(d) 22/02/2020 21:04:53 UT, ASI: LYR (557.7 nm)

(e) 22/02/2020 21:23:23 UT, ASI: LYR (557.7 nm)

(f) 22/02/2020 21:24:38 UT, ASI: LYR (557.7 nm)

(g) 22/02/2020 21:25:52 UT, ASI: LYR (557.7 nm)

(h) 22/02/2020 21:32:38 UT, ASI: LYR (557.7 nm)

Fig. 6. The aurora shown in this figure is classified as bands. The projection of the 557.7 nm emissions shown together with the phase scintillation index σ_ϕ over a map of Svalbard and geographical longitude/latitude on 22 February 2020 as seen from the LYR ASC for different time instances. Brighter yellow auroral emissions mean stronger intensity and bigger markers mean stronger σ_ϕ. The markers represent σ_ϕ measurements from NYA in red, LYR in green, HOR in cyan, HOP in magenta, and BJN in orange. Panel a shows a band-shaped Aurora and elevated σ_ϕ values west-ward. Panel b shows the intensified band, no with even stronger σ_ϕ values. Panels c and d show the fading of the auroral band, however σ_ϕ is still elevated. Panel e shows the commencement of the next auroral band, yet without strong elevated σ_ϕ values. Panels f and g show stronger auroral emissions paired with elevated σ_ϕ values at the boundary of the auroral band. In panel h elevated σ_ϕ is observed poleward of the fading auroral band.

selected substorm event (28 October 2019) shows arcs. For the first observed arc, we found a delay in the onset of elevated σ_ϕ values of 2 min, from when auroral activity (<30 kR) was observed (see again Figs. 4a–4c). The very strongly elevated σ_ϕ values are then observed at the poleward edge of the arc (Figs. 4d–4f) and between multiple arcs (Figs. 4e and 4f). Even for faint aurora, very strongly elevated, σ_ϕ values are measured for at least 2 min after the auroral intensity has decreased to under 60 kR, Figures 4g and 4h, the moderately elevated σ_ϕ values are observed for over 4 min after. In the substorm event on 29 January 2020, an auroral spiral was observed. For the spiral, the intensity is not monotonically increasing as it was for the arc. Moderately elevated σ_ϕ values are observed even for faint Aurora (<30 kR) (see again Figs. 5a). The elevated σ_ϕ values are observed on the edges of the auroral spiral (see Figs. 5c–5e). Over 10 min after the auroral intensity decreases under 60 kR very strongly elevated σ_ϕ values are still measured (see Fig. 5f). The last of the studied substorm events (22 February 2020) shows auroral bands. The abrupt and fluctuating intensity during the onset of the band causes auroral emissions with elevated σ_ϕ to be observed right away without a delay (see Fig. 6a). The second band first shows emissions above 60 kR and it takes over a minute to observe elevated σ_ϕ values (see Fig. 6e). For both bands, we observe elevated σ_ϕ values at the poleward boundary of the auroral form (see Figs. 6b, 6d and 6f, 6g). For the first band elevated σ_ϕ values are observed also at the west-ward boundary and within the form (see Fig. 6b). When the auroral bands fade out, elevated σ_ϕ values are still observed over 1–7 min (first and second example, respectively) (see Figs. 6c, 6d and 6g, 6h).

In summary, we observed: (1) Elevated phase scintillation index values correspond consistently well with the spatial and temporal evolution of auroral forms in the green emissions (oxygen, 557.7 nm) altitudes, which means particle precipitation into the ionospheric E-region is a driver for plasma structuring. (2) There may be a time delay between the temporal evolution of aurora (e.g., commencement and fading of auroral activity) and elevated phase scintillation index measurements. (3) The elevated phase scintillation index values are observed at the boundary of the auroral emissions (poleward for discrete and stable arcs and on all boundaries for bands and spirals).

When the ionospheric piercing point for the navigation satellites is chosen at the same altitude as the projections of the green (557.7 nm) auroral emissions, the elevated σ_ϕ values are consistently observed on the auroral edges. The same behavior is found when using only the co-located ASC and scintillation receiver (see the video with data from the NYA ASC and scintillation receiver in Supplementary material), a case where the mapping altitude becomes irrelevant. Thus we suggest the σ_ϕ values to affected at the altitude of the green auroral emissions. This means that E-region irregularities and instabilities cause observed plasma structuring. The findings are in agreement with Kinrade et al. (2013) and Semeter et al. (2017), also find a better correlation between observed elevated phase scintillation index values with the 557.7 nm auroral emissions.

Previous studies (e.g., van der Meeren et al., 2014; Jin et al., 2016) linked phase scintillation mainly to the polar cap F-region ionosphere (especially to polar cap patches and tongues of ionization). The effects of intense local particle precipitation in the auroral oval on elevated σ_ϕ have been studied and referred to as a blobs type II by Jin et al. (2016). They also state that soft F-region particle precipitation does not contribute much to plasma structuring processes in the nightside auroral region. Our findings are in agreement with this, but we, however, show that more energetic particle precipitation penetrating down to the E-region may be the main source and is found co-located with intense elevated σ_ϕ. The link between elevated σ_ϕ or phase scintillations and E-region auroral particle precipitation has also been observed by several authors (e.g., Kinrade et al., 2013; Forte et al., 2017; Loucks et al., 2017; Sreenivash et al., 2020; Datta-Barua et al., 2021; Makarevich et al., 2021).

The time delay strongly depends on the auroral dynamics with regard to auroral intensity. For a case where the aurora appears out of quiet conditions and the auroral intensity increases monotonically, the phase scintillation index values are elevated around 1 (2) minutes after the intensity reached over 60 kR (30 kR), see again the example of the auroral arc or the second auroral band. This is at a level on which simultaneous and co-located aurora and phase scintillation index enhancements are commonly found, even without further increases to higher intensity levels. The duration time delay depends strongly on which intensity is used as a threshold. When the auroral intensity is increasing (decreasing) non-monotonically, the time delay maybe even longer (shorter). In the case of the spiral, or, the first auroral band considered, the elevated σ_ϕ is observed right after a prompt increase in auroral intensity.

As the auroral intensity decreases monotonically, elevated σ_ϕ is observed down to levels of under 20 kR. Especially when the auroral intensity is fluctuating around these levels, we observe occasionally highly elevated scintillation index values. We have observed elevated σ_ϕ between 1 to over 7 min after auroral intensities dropped back under 60 kR. The effect of a time delay after decreasing auroral emissions is stronger than the time delay of the elevated σ_ϕ value onset. Both may only be reached for certain conditions. For stable forms, the relation may be more clear than for dynamic forms.

Particle precipitation is a signature observed as a part of field-aligned currents (Carter et al., 2016; Xiong et al., 2020). They couple the magnetosphere to the ionosphere and can cause severe phase scintillations through direct driving of the ionospheric plasma by structured precipitation or electric fields resulting in elevated scintillation index values (Boström, 1964; Fæhn Follestad et al., 2020). Particle precipitation is usually observed in times of high convection and convection patterns were investigated with SuperDARN. We see a two-cell pattern (during southward Bz) for the studied dates. We do not observe strong flows on the nightside, and experience mostly growth in the cells, linking to dayside reconnection (Dungey, 1961; Juusola et al., 2014). The negative By component is prominent for 29 January 2020, peaking at 22:00 UT the time we observe the spiral form, and is driving an asymmetric ionospheric convection pattern (e.g., Weimer, 1995). During times of particle precipitation, the twin cell convection pattern covers Svalbard and with this precipitation area.

We propose that the time delay may occur through a "memory effect". Particle precipitation into the ionospheric E-region enhances conductance and causes a widespread irregularity dissipation and redistribution of energy (e.g., Ivarsen et al., 2021). The influx of particles increases the plasma density leading to ionization and prolonging recombination. When the particle precipitation declines or moves, it will still take some time for plasma structures to diffuse. The structuring process initiated during particle precipitation will carry on. Instabilities in the plasma leading to further structuring processes, irregularity dissipation, and redistribution of energy.

The location of the elevated phase scintillation index values is also dependent on the spatial and temporal auroral dynamics. When investigating a stable discrete auroral form, such as the arc, we observe strongly elevated σ_ϕ (>0.5 rad) solely at the poleward boundary. If the form is faster moving, such as for spirals or bands, elevated σ_ϕ may be seen even westward or equatorward, but nevertheless on the boundaries. Fast-moving forms may move away quicker from the measurement location while elevated σ_ϕ value are still observed at this location. For spirals and bands, elevated σ_ϕ are observed also on the east and westward boundaries as well as on the boundaries within the shape. Semeter et al. (2017) studied the loss of lock (LL) events and their correlation with discrete auroral emissions. They studied mostly fast-moving auroral forms, and found LL events on equatorward (trailing) edge of the auroral form while the form is moving poleward. This agrees with our results, as we propose that there is a time delay in the elevated scintillation index measurements. Therefore, for fast-moving poleward forms, the LL events would be observed equatorward as the form moved past the measurement location further poleward. They note that although the poleward side of the arc has a similar or even greater density gradient, no LL events were observed there. This explanation may be valid in our case, as we propose that the structuring process in fact happens poleward, but the fast-moving form has simply moved from its original place as the structuring persists. This however would not explain the cases where we observe poleward elevated σ_ϕ values at multiple stable arcs, as the equatorward edge of the most poleward arc has a higher density gradient than the poleward boundary of an equatorward arc. Unless the equatorward arcs are sufficiently more intense than the poleward arcs, then the density gradient would be higher on the poleward edge of equatorward arcs (see Figs. 4e and 4f with two arcs).

The energy source for driving instabilities in the E-region ionosphere can be manifold, such as from flow shears, from gradients, or directly by kinetic energy. Instabilities associated with particle precipitation are, e.g., kinetic instabilities and two-stream instabilities. The flow of particles in field-aligned currents can also produce current-driven instabilities (e.g., Kropotkin, 2016).

One instability that can be directly produced by a velocity shear (by particle precipitation/electron beam) along the direction of or perpendicular to an externally imposed magnetic field is the Kelvin-Helmholtz instability (D'Angelo & Goeler, 1966; Hallinan & Davis, 1970; Pécseli, 2020). It can drive curls or spirals as observed in the aurora (Hallinan & Davis, 1970).

Another relevant instability that may explain the observed plasma structuring is the Farley-Buneman instability (Buneman, 1963; Farley Jr., 1963; Treumann, 1997). The instability arises from the difference in the electron and ion velocity, caused by collisions of the ions with neutrals (Farley Jr., 1963). These conditions are given in the equatorial and polar E-region ionosphere, where this instability is typically found (Rogister & D'Angelo, 1970; Pécseli, 2020).

Various instabilities can arise in the ionosphere driven by e.g., currents, energetic particle streams, or density gradients. However, the Kelvin-Helmholtz and Farley-Buneman instability do not only satisfy the encountered background conditions (E-region ionosphere, particle stream, collisions, availability of neutrals), but could also explain the observed behavior of elevated σ_ϕ observations at the edges of different auroral forms (spirals, arcs, bands) the boundaries between the injected particles and the ionospheric E-region plasma.

The Kelvin-Helmholtz instability is extracting energy out of a shear flow along a boundary (Treumann, 1997) and is associated with auroral spirals (Hallinan & Davis, 1970). This may explain why we measure elevated σ_ϕ values on the outer boundaries and boundaries within auroral spirals. The Farley-Buneman instability provides a more general explanation for plasma structuring observed at boundaries of different auroral forms, not only spirals. The auroral form boundaries are where the electrons stream past ions, which collide with neutrals, which is what feeds the Farley-Buneman instability (Buneman, 1963; Farley Jr., 1963). While the Kelvin-Helmholtz instability is working on bigger scales, the Farley-Buneman instability is operating on smaller scales. Multiple instabilities may be responsible for the plasma structuring processes we observe. Whether it is the difference in plasma density gradient that drives plasma structuring predominately at poleward edges of auroral arcs remains unknown. Further case studies with even higher spatial and temporal resolution are needed to understand the structuring process and to confirm which instability can cause delayed structuring processes in the E-region at the boundaries of auroral forms and at poleward boundaries for auroral arcs.

6 Conclusion

In this study, the relation between auroral particle precipitation and plasma structuring was investigated. In summary, the temporal and spatial evolution of auroral forms and phase scintillation index values were studied. For this, three-event days with similar background conditions (substorm events, particle precipitation, and nightside events) showing clear strong auroral emissions were selected. Data were available from three ASI imagers (NYA, LYR, and HOR) and five scintillation receivers (NYA, LYR and HOR, HOP, BJN). This provides us with 18 h of data in which we observed auroral forms such as arcs, spirals, and bands. Our results show that:

1. For the cases investigated by us elevated phase scintillation index values correspond to the spatial and temporal evolution of auroral forms when an ionospheric piercing point for navigation satellites is chosen the same as the estimated green emissions (557.7 nm) altitude (150 km). This suggests that plasma structuring in the ionospheric E-region is an important driver for phase scintillations.
2. We found a time delay between the temporal evolution of aurora (e.g. commencement and fading of auroral activity) and elevated phase scintillation index measurements. Particle precipitation enhances the plasma density. When the precipitation declines or moves, it will still take some time

for the plasma structures to diffuse. Until then, instabilities will further cause the redistribution of energy and irregularity dissipation.

3. The elevated phase scintillation index values are observed at the boundary of the auroral emissions. For discrete and stable arcs elevated phase scintillation index values are predominately observed poleward and for faster-moving shapes, including spirals and bands, on the boundaries of the form. The irregularities and instabilities causing the elevated phase scintillation index values, especially in the E-region may be due to instabilities that are driven by energy at the boundary of auroral forms, such as the Kelvin-Helmholtz instability (directly produced by a velocity shear such as from particle precipitation) or Farley-Buneman instability (through fast flows at the boundaries). Plasma structuring may predominately be observed on the poleward boundary as the gradient in plasma density is larger than it is on the equatorward boundary.

The question of why plasma structuring processes in the E-region are observed specifically at the edges of auroral forms, such as spirals and bands, and at poleward boundaries for auroral arcs open. Case studies only provide insight into a few well-studied examples of the plasma structuring processes in relation to different auroral forms. Further case studies with even higher spatial and temporal resolution and larger statistical studies investigating time-delay statistics are needed to understand the structuring process. In the future, we also need to investigate further, which instabilities are related to the plasma structuring processes and how they affect trans-ionospheric radio waves.

Supplementary materials

Supplementary material is available at https://www.swsc-journal.org/10.1051/swsc/2022038/olm

The projection of the 557.7 nm emissions shown together with the phase scintillation index over a map of Svalbard. Date, receiver location, and auroral form are indicated in the file names. Brighter yellow auroral emissions mean stronger intensity and bigger markers mean stronger phase scintillation index. The markers represent phase scintillation index measurements from NYA in red, LYR in green, HOR in cyan, HOP in magenta, and BJN in orange.

Video S1: 29012020_LYR_spiral_3fps.mp4
Video S2: 29012020_LYR_spiral_red_3fps.mp4
Video S3: NYA_arc_NYAreceiver_3fps.mp4
Video S4: 28102019_NYA_arc_3fps.mp4
Video S5: 28102019_LYR_arc_3fps.mp4
Video S6: 29012020_NYA_spiral_3fps.mp4
Video S7: 22022020 HOR bands 3fps.mp4
Video S8: 22022020 LYR bands 3fps.mp4
Video S9: 22022020 NYA bands 3fps.mp4

Acknowledgements. The authors thank Bjørn Lybekk for the maintenance of the all-sky imager and scintillation receiver data. The UiB Global Navigation Satellite System Data Collection was collected under Research Council of Norway contracts 212014 and 223252. Data from Hornsund have been acquired at the Polish Polar Station Hornsund in collaboration with the Institute of Geophysics, Polish Academy of Sciences. This study is in part supported by the European Research Council, under the European Union's Horizon-2020 research and innovation programe (Grant Agreement No. 866357, POLAR-4DSpace). We thank the institutes who maintain the IMAGE Magnetometer Array: Tromsø Geophysical Observatory of UiT the Arctic University of Norway (Norway), Finnish Meteorological Institute (Finland), Institute of Geophysics Polish Academy of Sciences (Poland), GFZ German Research Centre for Geosciences (Germany), Geological Survey of Sweden (Sweden), Swedish Institute of Space Physics (Sweden), Sodankylä Geophysical Observatory of the University of Oulu (Finland), and Polar Geophysical Institute (Russia). Florine Enengl would like to thank Noora Partamies for fruitful discussions. The editor thanks two anonymous reviewers for their assistance in evaluating this paper.

References

Akasofu S-I. 1965. Dynamic morphology of auroras. *Space Sci Rev* **4(4)**: 498. https://doi.org/10.1007/BF00177092

Akasofu S-I. 1966. The auroral oval, the auroral substorm, and their relations with the internal structure of the magnetosphere. *Planet Space Sci* **14(7)**: 587–595. https://doi.org/10.1016/0032-0633(66)90043-2.

Alfonsi L, Cilliers PJ, Romano V, Hunstad I, Correia E, et al. 2016. First observations of gnss ionospheric scintillations from DemoGRAPE project. *Space Weather* **14(10)**: 704–709. https://doi.org/10.1002/2016SW001488.

Alfonsi L, Kavanagh AJ, Amata E, Cilliers P, Correia E, et al. 2008. Probing the high latitude ionosphere from ground-based observations: The state of current knowledge and capabilities during IPY (2007–2009). *J Atmos Sol Terr Phys* **70(18, SI)**: 2293–2308. https://doi.org/10.1016/j.jastp.2008.06.013.

Basu S, Weber EJ, Bullett TW, Keskinen MJ, MacKenzie E, Doherty P, Sheehan R, Kuenzler H, Ning P, Bongiolatti J. 1998. Characteristics of plasma structuring in the cusp/cleft region at Svalbard. *Radio Sci* **33(6)**: 1885–1899. https://doi.org/10.1029/98RS01597.

Beach TL. 2006. Perils of the GPS phase scintillation index. *Radio Sci* **41(5)**. https://doi.org/10.1029/2005RS003356.

Boström R. 1964. A model of the auroral electrojets. *J Geophys Res* **69(23)**: 4983–4999. https://doi.org/10.1029/JZ069i023p04983.

Briggs B, Parkin I. 1963. On the variation of radio star and satellite scintillations with zenith angle. *J Atmos Terr Phys* **25(6)**: 339–366. https://doi.org/10.1016/0021-9169(63)90150-8.

Buneman O. 1963. Excitation of field aligned sound waves by electron streams. *Phys Rev Lett* **10(7)**: 285–287. https://doi.org/10.1103/PhysRevLett.10.285.

Carter JA, Milan SE, Coxon JC, Walach M-T, Anderson BJ. 2016. Average field-aligned current configuration parameterized by solar wind conditions. *J Geophys Res Space Physics* **121(2)**: 1294–1307. https://doi.org/10.1002/2015JA021567.

Chernyshov AA, Miloch WJ, Jin Y, Zakharov VI. 2020. Relationship between TEC jumps and auroral substorm in the high-latitude ionosphere. *Sci Rep* **10**: 6363. https://doi.org/10.1038/s41598-020-63422-9.

D'Angelo N, Goeler SV. 1966. Investigation of the Kelvin-Helmholtz Instability in a Cesium Plasma. *Phys Fluids* **9(2)**: 309–313. https://doi.org/10.1063/1.1761674.

Datta-Barua S, Llado Prat P, Hampton DL. 2021. Multiyear detection, classification and hypothesis of ionospheric layer causing GNSS scintillation. *Radio Sci* **56(12)**: e2021RS007328. https://doi.org/10.1029/2021RS007328.

Davis T. 1978. Observed characteristics of auroral forms. *Space Sci Rev* **22(1)**: 77–113. https://doi.org/10.1007/BF00215814.

Davis TN, Hallinan TJ. 1976. Auroral spirals, 1. Observations. *J Geophys Res* **81(22)**: 3953–3958. https://doi.org/10.1029/JA081i022p03953.

Deshpande KB, Bust GS, Clauer CR, Rino CL, Carrano CS. 2014. Satellite-beacon ionospheric-scintillation global model of the upper atmosphere (SIGMA) I: High-latitude sensitivity study of the model parameters. *J Geophys Res Space Phys* **119(5)**: 4026–4043. https://doi.org/10.1002/2013JA019699.

D'Onofrio M, Partamies N, Tanskanen E. 2014. Eastward electrojet enhancements during substorm activity. *J Atmos Sol Terr Phys* **119**: 129–137. https://doi.org/10.1016/j.jastp.2014.07.007.

Dungey JW. 1961. Interplanetary magnetic field and the auroral zones. *Phys Rev Lett* **6(2)**: 47–48. https://doi.org/10.1103/PhysRevLett.6.47.

Elphinstone RD, Murphree JS, Cogger LL. 1996. What is a global auroral substorm? *Rev Geophys* **34(2)**: 169–232. https://doi.org/10.1029/96RG00483.

Farley Jr. DT. 1963. A plasma instability resulting in field-aligned irregularities in the ionosphere. *J Geophys Res* **68(22)**: 6083–6097. https://doi.org/10.1029/JZ068i022p06083.

Fæhn Follestad A, Herlingshaw K, Ghadjari H, Knudsen DJ, McWilliams KA, Moen JI, Spicher A, Wu J, Oksavik K. 2020. Dayside field-aligned current impacts on ionospheric irregularities. *Geophys Res Lett* **47(11)**: e2019GL086722. https://doi.org/10.1029/2019GL086722.

Forte B, Coleman C, Skone S, Häggström I, Mitchell C, Da Dalt F, Panicciari T, Kinrade J, Bust G. 2017. Identification of scintillation signatures on GPS signals originating from plasma structures detected with EISCAT incoherent scatter radar along the same line of sight. *J Geophys Res Space Phys* **122(1)**: 916–931. https://doi.org/10.1002/2016JA023271.

Gillies DM, Knudsen DJ, Donovan EF, Spanswick EL, Hansen C, Keating D, Erion S. 2014. A survey of quiet auroral arc orientation and the effects of the interplanetary magnetic field. *J Geophys Res Space Phys* **119(4)**: 2550–2562. https://doi.org/10.1002/2013JA019469.

Hallinan TJ. 1976. Auroral spirals, 2. Theory. *J Geophys Res* **81(22)**: 3959–3965. https://doi.org/10.1029/JA081i022p03959.

Hallinan TJ, Davis T. 1970. Small-scale auroral arc distortions. *Planet Space Sci* **18(12)**: 1735–1736. https://doi.org/10.1016/0032-0633(70)90007-3.

Hey JS, Parsons SJ, Phillips JW. 1946. Fluctuations in cosmic radiation at radio-frequencies. *Nature (London)* **158(4007)**: 234–234. https://doi.org/10.1038/158234a0.

Huba JD, Hassam AB, Schwartz IB, Keskinen MJ. 1985. Ionospheric turbulence: Interchange instabilities and chaotic fluid behavior. *Geophys Res Lett* **12(1)**: 65–68. https://doi.org/10.1029/GL012i001p00065.

Ivarsen MF, St-Maurice J-P, Jin Y, Park J, Miloch W, Spicher A, Kwak Y-S, Clausen LBN. 2021. Steepening plasma density spectra in the ionosphere: The crucial role played by a strong E-region. *J Geophys Res Space Phys* **126(8)**: e2021JA029401. https://doi.org/10.1029/2021JA029401.

Ivchenko N, Blixt EM, Lanchester BS. 2005. Multispectral observations of auroral rays and curls. *Geophys Res Lett* **32(18)**: L18106. https://doi.org/10.1029/2005GL022650.

Jin Y, Moen JI, Miloch WJ, Clausen LBN, Oksavik K. 2016. Statistical study of the GNSS phase scintillation associated with two types of auroral blobs. *J Geophys Res Space Phys* **121(5)**: 4679–4697. https://doi.org/10.1002/2016JA022613.

Jin Y, Moen JI, Oksavik K, Spicher A, Clausen LB, Miloch WJ. 2017. GPS scintillations associated with cusp dynamics and polar cap patches. *J Space Weather Space Clim* **7**: A23. https://doi.org/10.1051/swsc/2017022.

Juusola L, Milan SE, Lester M, Grocott A, Imber SM. 2014. Interplanetary magnetic field control of the ionospheric field-aligned current and convection distributions. *J Geophys Res Space Phys* **119(4)**: 3130–3149. https://doi.org/10.1002/2013JA019455.

Karlsson T, Andersson L, Gillies D, Lynch K, Marghitu O, Partamies N, Sivadas N, Wu J. 2020. Quiet, discrete auroral arcs – observations. *Space Sci Rev* **216(1)**. https://doi.org/10.1007/s11214-020-0641-7.

Keiling A, Angelopoulos V, Weygand J, Amm O, Spanswick E, et al. 2009. THEMIS ground-space observations during the development of auroral spirals. *Ann Geophys* **27(11)**: 4317–4332. https://doi.org/10.5194/angeo-27-4317-2009.

Kelley MC, Vickrey JF, Carlson CW, Torbert R. 1982. On the origin and spatial extent of high-latitude F region irregularities. *J Geophys Res Space Phys* **87(A6)**: 4469–4475. https://doi.org/10.1029/JA087iA06p04469.

Keskinen MJ, Ossakow SL. 1983. Theories of high-latitude ionospheric irregularities: A review. *Radio Sci* **18(6)**: 1077–1091. https://doi.org/10.1029/RS018i006p01077.

King J, Papitashvili N. 2005. Solar wind spatial scales in and comparisons of hourly Wind and ACE plasma and magnetic field data. *J Geophys Res* **A02104**: 110. https://doi.org/10.1029/2004JA010649.

Kinrade J, Mitchell CN, Smith ND, Ebihara Y, Weatherwax AT, Bust GS. 2013. GPS phase scintillation associated with optical auroral emissions: First statistical results from the geographic South Pole. *J Geophys Res Space Phys* **118(5)**: 2490–2502. https://doi.org/10.1002/jgra.50214.

Kintner P, Ledvina B, Kintner PM, Ledvina BM. 2005. The ionosphere, radio navigation, and global navigation satellite systems. *Adv Space Res* **35(5)**: 788–811. https://doi.org/10.1016/j.asr.2004.12.076.

Kintner PM, Ledvina BM, de Paula ER. 2007. GPS and ionospheric scintillations. *Space Weather* **5(9)**: S09003. https://doi.org/10.1029/2006SW000260.

Kintner PM, Seyler CE. 1985. The status of observations and theory of high latitude ionospheric and magnetospheric plasma turbulence. *Space Sci Rev* **41(1–2)**: 91–129. https://doi.org/10.1007/BF00241347.

Knudsen DJ, Donovan EF, Cogger LL, Jackel B, Shaw WD. 2001. Width and structure of mesoscale optical auroral arcs. *Geophys Res Lett* **28(4)**: 705–708. https://doi.org/10.1029/2000GL011969.

Kropotkin A. 2016. Formation of the small-scale structure of auroral electron precipitations. *J Atmos Sol Terr Phys* **148**: 39–47. https://doi.org/10.1016/j.jastp.2016.08.009.

Loucks D, Palo S, Pilinski M, Crowley G, Azeem I, Hampton D. 2017. High-latitude GPS phase scintillation from E region electron density gradients during the 20–21 December 2015 geomagnetic storm. *J Geophys Res Space Phys* **122(7)**: 7473–7490. https://doi.org/10.1002/2016JA023839.

Makarevich RA, Crowley G, Azeem I, Ngwira C, Forsythe VV. 2021. Auroral E-region as a source region for ionospheric scintillation. *J Geophys Res Space Phys* **126(5)**: e2021JA029212. https://doi.org/10.1029/2021JA029212.

Matzka J, Stolle C, Yamazaki Y, Bronkalla O, Morschhauser A. 2021. The geomagnetic Kp index and derived indices of geomagnetic activity. *Space Weather* **19(5)**: e2020SW002641. https://doi.org/10.1029/2020SW002641.

Millward GH, Moffett RJ, Balmforth HF, Rodger AS. 1999. Modeling the ionospheric effects of ion and electron precipitation in the cusp. *J Geophys Res Space Phys* **104(A11)**: 24603–24612. https://doi.org/10.1029/1999JA900249.

Moen JI, Oksavik K, Alfonsi L, Dåbakk YR, Romano V, Spogli L. 2013. Space weather challenges of the polar cap ionosphere. *J Space Weather Space Clim* **3**: A02. https://doi.org/10.1051/swsc/2013025.

Mrak S, Semeter J, Hirsch M, Starr G, Hampton D, et al. 2018. Field-aligned GPS scintillation: multisensor data fusion. *J Geophys Res Space Phys* **123(1)**: 974–992. https://doi.org/10.1002/2017JA024557.

Nikolaeva V, Gordeev E, Sergienko T, Makarova L, Kotikov A. 2021. AIM-E: E-region auroral ionosphere model. *Atmosphere* **12(6)**: 748. https://doi.org/10.3390/atmos12060748.

Oksavik K. 2020a. Documentation of GNSS total electron content and scintillation data (60 s) at svalbard. *DataverseNO*. https://doi.org/10.18710/EA5BYX.

Oksavik K. 2020b. The University of Bergen global navigation satellite system data collection. *DataverseNO*. https://doi.org/10.18710/AJ4S-X394.

Partamies N, Juusola L, Whiter D, Kauristie K. 2015. Substorm evolution of auroral structures. *J Geophys Res Space Phys* **120(7)**: 5958–5972. https://doi.org/10.1002/2015JA021217.

Partamies N, Kauristie K, Pulkkinen TI, Brittnacher M. 2001. Statistical study of auroral spirals. *J Geophys Res Space Phys* **106(A8)**: 15415–15428. https://doi.org/10.1029/2000JA900172.

Partamies N, Syrjäsuo M, Donovan E, Connors M, Charrois D, Knudsen D, Kryzanowsky Z. 2010. Observations of the auroral width spectrum at kilometre-scale size. *Ann Geophys* **28(3)**: 711–718. https://doi.org/10.5194/angeo-28-711-2010.

Partamies N, Weygand JM, Juusola L. 2017. Statistical study of auroral omega bands. *Ann Geophys* **35(5)**: 1069–1083. https://doi.org/10.5194/angeo-35-1069-2017.

Pécseli HL. 2020. *Waves and oscillations in plasmas. Series in plasma physics*. CRC Press. https://doi.org/10.1201/9780429489976.

Prikryl P, Spogli L, Jayachandran PT, Kinrade J, Mitchell CN, et al. 2011. Interhemispheric comparison of GPS phase scintillation at high latitudes during the magnetic-cloud-induced geomagnetic storm of 5–7 April 2010. *Ann Geophys* **29(12)**: 2287–2304. https://doi.org/10.5194/angeo-29-2287-2011.

Rogister A, D'Angelo N. 1970. Type II irregularities in the equatorial electrojet. *J Geophys Res* **75(19)**: 3879–3887. https://doi.org/10.1029/JA075i019p03879.

Semeter J, Mrak S, Hirsch M, Swoboda J, Akbari H, et al. 2017. GPS signal corruption by the discrete aurora: precise measurements from the mahali experiment. *Geophys Res Lett* **44(19)**: 9539–9546. https://doi.org/10.1002/2017GL073570.

Semeter J, Zettergren M, Diaz M, Mende S. 2008. Wave dispersion and the discrete aurora: New constraints derived from high-speed imagery. *J Geophys Res Space Phys* **113**: A12208. https//doi.org/10.1029/2008JA013122.

Skone S, Knudsen K, de Jong M. 2001. Limitations in GPS receiver tracking performance under ionospheric scintillation conditions. *Phys Chem Earth Part A* **26(6–8)**: 613–621. https://doi.org/10.1016/S1464-1895(01)00110-7.

Spogli L, Cesaroni C, Di Mauro D, Pezzopane M, Alfonsi L, et al. 2016. Formation of ionospheric irregularities over Southeast Asia during the 2015 St. Patrick's Day storm. *J Geophys Res Space Phys* **121(12)**: 12211–12233. https://doi.org/10.1002/2016JA023222.

Sreenivash V, Su Y, Datta-Barua S. 2020. Automated ionospheric scattering layer hypothesis generation for detected and classified auroral global positioning system scintillation events. *Radio Sci* **55 (1)**: e2018RS006779. https://doi.org/10.1029/2018RS006779.

Tanskanen E. 2009. A comprehensive high-throughput analysis of substorms observed by IMAGE magnetometer network: Years 1993–2003 examined. *J Geophys Res* **114**: A05204. https://doi.org/10.1029/2008JA013682.

Treumann RA. 1997. *Advanced space plasma physics*. Imperial College Press. https://doi.org/10.1142/p020.

van der Meeren C, Oksavik K, Lorentzen D, Moen JI, Romano V. 2014. GPS scintillation and irregularities at the front of an ionization tongue in the nightside polar ionosphere. *J Geophys Res Space Phys* **119(10)**: 8624–8636. https://doi.org/10.1002/2014JA020114.

van der Meeren C, Oksavik K, Lorentzen DA, Rietveld MT, Clausen LBN. 2015. Severe and localized GNSS scintillation at the poleward edge of the nightside auroral oval during intense substorm aurora. *J Geophys Res Space Phys* **120(12)**: 10607–10621. https://doi.org/10.1002/2015JA021819.

Wanliss JA, Showalter KM. 2006. High-resolution global storm index: Dst versus SYM-H. *J Geophys Res Space Phys* **111(A2)**. https://doi.org/10.1029/2005JA011034.

Weber EJ, Tsunoda RT, Buchau J, Sheehan RE, Strickland DJ, Whiting W, Moore JG. 1985. Coordinated measurements of auroral zone plasma enhancements. *J Geophys Res Space Phys* **90(A7)**: 6497–6513. https://doi.org/10.1029/JA090iA07p06497.1.

Weimer DR. 1995. Models of high-latitude electric potentials derived with a least error fit of spherical harmonic coefficients. *J Geophys Res* **100(A10)**: 19595–19607. https://doi.org/10.1029/95JA01755.

Wilson GR, Weimer DR, Wise JO, Marcos FA, Wilson GR, Weimer DR, Wise JO, Marcos FA. 2006. Response of the thermosphere to Joule heating and particle precipitation. *J Geophys Res* **111(A10)**. https://doi.org/10.1029/2005JA011274.

Xiong C, Stolle C, Alken P, Rauberg J. 2020. Relationship between large-scale ionospheric field-aligned currents and electron/ion precipitations: DMSP observations. *Earth Planets Space* **72(1)**: 1–22. https://doi.org/10.1186/s40623-020-01286-z.

Yeh KC, Liu C-H. 1982. Radio wave scintillations in the ionosphere. *Proc IEEE* **70(4)**: 324–360. https://doi.org/10.1109/PROC.1982.12313.

Cite this article as: Enengl F, Kotova D, Jin Y, Clausen LBN & Miloch WJ. 2023. Ionospheric plasma structuring in relation to auroral particle precipitation. *J. Space Weather Space Clim.* **13**, 1. https://doi.org/10.1051/swsc/2022038.

Paper II

Investigation of Ionospheric Small-Scale Plasma Structures associated with Particle Precipitation

Florine Enengl, Luca Spogli, Daria Kotova, Yaqi Jin, Kjellmar Oksavik, Noora Partamies, Wojciech J. Miloch

Submitted for publication. DOI: 10.22541/essoar.168748399.90008606/v1.

Paper III

Electron Temperature Inference from Multiple Fixed Bias Langmuir Probes

Florine Enengl, Sigvald Marholm, Sayan Adhikari, Richard Marchand, Wojciech J. Miloch

Submitted for publication. DOI: 10.1002/essoar.10512804.1.